

Princeton/HEP/94-01  
March 22, 1994  
Second Draft

## Hadron Identification for B Physics

Z. Cheng, C. Lu, D.R. Marlow, K.T. McDonald and E. Prebys

*Joseph Henry Laboratories, Princeton University, Princeton, NJ 08544*

### Abstract

We review our ongoing R&D program whose goal is to identify the best options for  $\pi/K$  separation in  $B$ -physics experiments by the end of calendar 1994. Studies are proceeding on three types of detectors, two of which incorporate UV-sensitive CsI photocathodes that can be made at modest cost in physicists' laboratories: aerogel threshold Čerenkov counters, and RICH detectors. The third technology is a time-of-flight system based on multichannel-plate photomultipliers (MCP-PMT's) that view Čerenkov radiation in quartz fibers; the anticipated time resolution of 30 ps permits  $\pi/K$  separation up to 5 GeV/ $c$ . A supplementary budget of \$80k is proposed to continue these studies in 1994.

# Contents

<b>1</b>	<b>Introduction</b>	<b>1</b>
1.1	Do We Need Hadron ID for $P_t > 1.5 \text{ GeV}/c$ ?	1
1.2	Hadron ID Technologies	2
<b>2</b>	<b>A Čerenkov Time-of-Flight System with MCP-PMT's</b>	<b>3</b>
2.1	Use of Optical Fiber Hoops as a Delay Line	5
2.1.1	The Need for Two Layers of Fibers	6
2.1.2	Multiple Hits	7
2.2	MCP-PMT Issues	8
2.2.1	Rate Limitations	8
2.2.2	MCP Lifetime	8
2.2.3	Backgrounds	9
2.2.4	MCP-PMT's with Larger Active Area	12
2.3	Fiber Issues	12
2.3.1	Mechanical Integrity	12
2.3.2	Cost	13
2.3.3	Mechanical Assembly	13
2.3.4	Dispersion in the Fiber	14
2.3.5	Čerenkov Light in a Circular Fiber	15
2.3.6	Fluorescence and Radiation Damage	17
<b>3</b>	<b>Threshold Čerenkov Counters with Aerogel Radiators and CsI Photocathodes</b>	<b>17</b>
<b>4</b>	<b>Fast RICH Detector with CsI Photocathode</b>	<b>19</b>
4.1	Quantum Efficiency of a CsI photocathode	20
4.2	Dependence of the Quantum Efficiency on Temperature	23
4.3	Use of Ceramic Substrates	25
4.4	The Need for Precharging of CsI Photocathodes	25
4.5	Aging of CsI Photocathodes by Charge Transport	25
4.6	Wire <i>vs.</i> Mesh Anodes: Electric-Field Dependence of the Quantum Efficiency	27
4.7	Charge Sharing on the Cathode Readout Pads	30
4.8	Analog <i>vs.</i> Digital Readout	32
4.9	Tilted RICH Modules	36
4.10	Backgrounds	38
<b>5</b>	<b>R&amp;D Proposal</b>	<b>39</b>
5.1	R&D Goals	39
5.1.1	Time-of-Flight System	39
5.1.2	Aerogel + CsI Threshold Čerenkov Counters	39
5.1.3	RICH Detector with CsI Photocathode	40
5.2	Personnel	40
5.3	Proposed Budget for FY94	41

5.4	Milestones . . . . .	41
5.4.1	Time-of-Flight System . . . . .	41
5.4.2	Aerogel + CsI Threshold Čerenkov Counters . . . . .	42
5.4.3	RICH Detectors with CsI Photocathodes . . . . .	42
6	References . . . . .	43

## List of Figures

1	Quality of $\pi/K$ separation in a time-of-flight system. . . . .	3
2	MCP performance in magnetic fields. . . . .	4
3	Optical delay line for Čerenkov light. . . . .	5
4	Hoops of Čerenkov radiators. . . . .	6
5	Capability of a Čerenkov time-of-flight system. . . . .	7
6	Lifetime of an MCP-PMT. . . . .	9
7	Charged-particle backgrounds. . . . .	10
8	X-ray backgrounds from spent positrons and Bhabhas. . . . .	11
9	X-ray backgrounds from synchrotron radiation. . . . .	11
10	Wavelength spectrum of all detected Čerenkov photons. . . . .	14
11	Wavelength spectrum of the earliest detected Čerenkov photons. . . . .	15
12	Optical path length of the earliest Čerenkov photons. . . . .	16
13	UV transmission in quartz. . . . .	18
14	Sketch of the VUV monochromator. . . . .	21
15	Comparison of a calibrated diode and PMT. . . . .	22
16	Calibration of a VUV beam splitter. . . . .	23
17	Quantum efficiency of CsI photocathodes. . . . .	24
18	Photocurrent <i>vs.</i> temperature for a fresh-made CsI photocathode. . . . .	25
19	Photocurrent <i>vs.</i> collected charge for a CsI photocathode in vacuum. . . . .	26
20	A RICH prototype with an anode-wire plane. . . . .	28
21	Gain spectra in a MWPC. . . . .	28
22	Dependence of the quantum efficiency on $E/P$ . . . . .	29
23	Design of a RICH photodetector with wire anode. . . . .	31
24	The Polya distribution for single-electron avalanches. . . . .	32
25	True <i>vs.</i> reconstructed position in the pad chamber. . . . .	33
26	Error in the reconstructed position in the pad chamber. . . . .	34
27	Charge-sharing measurements. . . . .	35
28	Mechanical layout of the RICH readout electronics. . . . .	35
29	Block diagram of the RICH front-end electronics. . . . .	36
30	Block diagram of the RICH off-detector electronics. . . . .	36
31	A RICH detector with tilted radiators. . . . .	37

## List of Tables

1	Performance of aerogel + CsI. . . . .	19
2	Proposed R&D Budget for FY1994. . . . .	41

# 1 Introduction

$B$ -physics experiments with the goal of measuring  $CP$  violation have been discussed since at least 1984 [1, 2], but only in the last few months have realistic plans emerged to pursue these experiments at Fermilab [3], KEK [4] and SLAC [5]. Among the types of detector technology needed for these experiments, only that for hadron identification is not well determined at the present time.

Based on current understanding, there is considerable risk in choosing a single technology that must meet all hadron ID needs; yet the ambitious spirit with which  $B$ -physics experiments are being proposed favors an all-inclusive solution. In the coming months it will be prudent to examine the match between goals and capabilities carefully.

In this Introduction we review the physics requirements for  $\pi/K$  separation, and then comment on the technology options we feel are most promising. In the following sections we give details as to present knowledge and plans for future R&D.

## 1.1 Do We Need Hadron ID for $P_t > 1.5$ GeV/ $c$ ?

The most prominent need for hadron ID in studies of  $CP$  violation in the  $B$ -meson system is for flavor tagging of the second  $B$  in events containing a neutral  $B$  that decays to a self-conjugate final state. The decay chain  $b \rightarrow c \rightarrow s$  occurs with near unit probability for the second  $B$ , leading to charged Kaons whose sign tags the flavor of the  $B$  correctly in about 45% ( $= P(\text{right}) - P(\text{wrong})$ ) of all decays. Note that side branch  $b \rightarrow W^- \rightarrow \bar{c}s$  leads to the same flavor Kaon; only the low- $P_t$ , Cabibbo-suppressed side branch  $c \rightarrow W^+ \rightarrow u\bar{s}$  leads to a wrong-sign Kaon.

The momentum spectrum of Kaons from the second  $B$  is soft, and there are rapidly diminishing returns for  $P_t > 1.5$  GeV/ $c$ .

Motivation for hadron ID at larger  $P_t$  comes from the desire to reconstruct exclusive channels such as  $B^0 \rightarrow \pi^+\pi^-$ ,  $K^+\pi^-$  and  $K^+K^-$  (as well as channels not particularly relevant to  $CP$  violation such as  $B \rightarrow \pi(K)\tau\nu$ ). Here the  $P_t$  spectra extends to about 4.5 GeV/ $c$ .

Particularly at an  $e^+e^-$  collider there is limited need for hadron ID to untangle the two-body decays of the  $B_d^0$  as there is no background from  $B_s^0$  (for which the branch to  $K\pi$  is about the same as for  $B_d^0 \rightarrow \pi\pi$ , and whose mass is close to  $m_{B_d} + m_\pi$ ). In tree diagrams,  $B_d^0 \rightarrow K\pi$  is Cabibbo suppressed compared to  $B_d^0 \rightarrow \pi\pi$ , and a misidentified  $K$  leads to a reconstructed mass for the  $B$  at least  $m_\pi$  below the true value. Hence if the  $B$ -mass resolution is small compared to  $m_\pi$ , there is little need for hadron ID in studies of  $B_d \rightarrow \pi\pi$  at an  $e^+e^-$  collider unless the  $K\pi$  branch greatly exceeds that for  $\pi\pi$ , in contrast to standard expectations.

Some concern has arisen in the past years because CLEO does yet show that the decay  $B_d \rightarrow K\pi$  is indeed suppressed compared to the  $\pi\pi$  mode. In penguin graphs leading to these states the  $K\pi$  mode is Cabibbo favored, so in extreme scenarios the  $K\pi$  mode might be favored. (If so, the penguin contamination of the  $\pi\pi$  mode would greatly reduce its utility for studies of the phase of the C-K-M matrix element  $V_{ub}$ .) The recent observation of penguin decays at CLEO [6] at almost exactly the branch predicted in standard calculations suggests that the penguin contribution to  $B_d \rightarrow K\pi$  is small compared to the tree contribution to

$B_d \rightarrow \pi\pi$ . In this context the need for hadron ID for  $P_t > 1.5$  GeV/ $c$  is more as a precaution against surprises than an obvious critical issue.

A major debate is how much to put the detector at risk to provide hadron ID for the range  $1.5 < P_t < 4.5$  GeV/ $c$ .

For central detectors, the relatively conventional technologies of  $dE/dx$  plus time-of-flight scintillators suffice to provide good hadron ID up to about 1.5 GeV/ $c$ . Both Fermilab and KEK (as well as CLEO) propose to base their particle ID strategies on these technologies, with higher  $P_t$  coverage as a speculative option. The SLAC proposal is distinguished in that the nominal scenario dispenses with time-of-flight counters altogether. The SLAC strategy is driven in part by the concern that the CsI calorimeter is 50% of the total cost of the detector, and its performance would be degraded somewhat by the increased material of two hadron ID systems preceding it; yet the CsI calorimeter plays only a modest role in studies of  $CP$  violation.

## 1.2 Hadron ID Technologies

In our view, three hadron ID technologies remain as serious contenders for implementation at the B-physics experiments, and deserve additional R&D to clarify their role:

1. Time-of-flight counters.
2. Threshold Čerenkov counters (with  $dE/dx$  measurements for low- $P_t$  coverage).
3. RICH detectors.

A time-of-flight system is appealing in that the capability for  $\pi/K$  separation up to  $P \sim 1.5$  GeV/ $c$  has already been demonstrated [4] for a system of scintillators viewed by conventional photomultipliers. Our interest is in exploring a potential fourfold improvement in time resolution, which would double the momentum coverage. The technology for this would be photomultipliers with a bialkali photocathode and a two-stage microchannel plate (so-called MCP-PMT's), which detect Čerenkov light from quartz bars.

This scheme has the potential for an even more extended range of  $\pi/K$  separation due to the differing flight paths of light from  $\pi$ 's and  $K$ 's, as suggested by Selen [7]. If the radiators are hoops of quartz fibers rather than longitudinal bars it should be possible to achieve  $\pi/K$  separation up to 5 GeV/ $c$ . Such a system would cost \$2-3M.

A time-of-flight system would also serve at an  $e^+e^-$  collider to identify in which rf bucket (period = 4 ns) the event occurred, as needed for precision drift-chamber tracking [8].

A threshold Čerenkov counter can provide  $\pi/K$  separation over a momentum range of a factor of three. Assuming a  $dE/dx$  measurement provides  $\pi/K$  separation up to 500 MeV/ $c$ , one Čerenkov counter with index 1.008 could cover the range  $0.5 < P < 1.5$  GeV/ $c$ , and another with index 1.06 could cover the range  $1.5 < P < 4.5$  GeV/ $c$ . This is another simple scheme that could provide coverage out to 4.5 GeV/ $c$ . Aerogels of the required index appear feasible using the 'two-step' production technique of Hrubesh [9]. However, suitable commercial photodetectors for operation in a 1-1.5-T magnetic field will cost \$1.5-2k each, so the cost for the desired 8,000 or so cells is high. We wish to explore the coupling of low-cost CsI photocathodes to aerogels. This puts a premium on UV transparency for the aerogels, which has not been well studied.

The most ambitious solution for hadron ID is a RICH detector. Serious questions remain as to whether the quantum efficiency and lifetime are sufficient in production detectors based on CsI photocathodes. We have been working on these issues for two years, and will continue our studies in FY94.

While the DIRC option [10, 11] is not part of our R&D plans, we encourage its proponents to pursue it in a timely manner.

## 2 A Čerenkov Time-of-Flight System with MCP-PMT's

For  $\pi$ - $K$  separation, the time-of-flight difference over a path length  $L$  is

$$\Delta t[\text{ps}] = \frac{L}{c} \left( \sqrt{1 + M_K^2/P^2} - \sqrt{1 + M_\pi^2/P^2} \right) \sim \frac{L}{c} \frac{M_K^2 - M_\pi^2}{2P^2} \sim \frac{3.75L[\text{cm}]}{P[\text{GeV}/c]^2}.$$

If we desire a separation of  $N$  standard deviations in a system with r.m.s. time resolution  $\sigma_t$ , the maximum transverse momentum at which this separation holds is given by

$$P_{\text{max}} \approx \sqrt{\frac{3.75L[\text{cm}]}{N\sigma_t[\text{ps}]}} ,$$

as shown in Fig. 1.

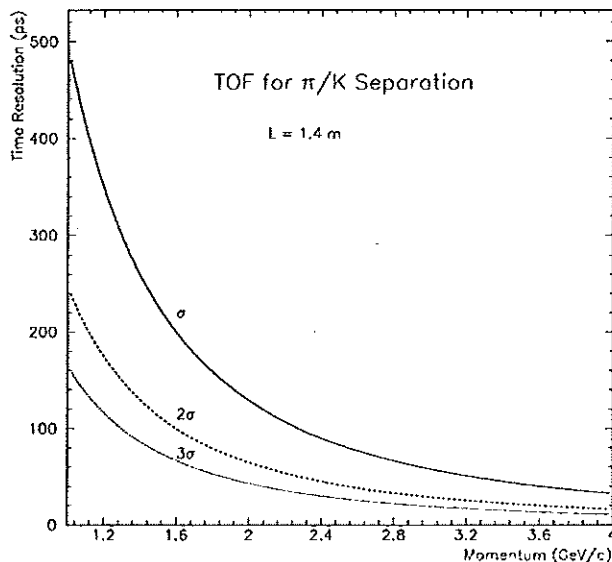


Figure 1: The statistical significance of  $\pi/K$  separation by a time-of-flight system with path length 1.4 m as a function of momentum and time resolution.

A time-of-flight system based on scintillator and Hamamatsu fine-mesh photomultipliers has been demonstrated to yield time resolutions of  $\sigma_t = 100$  ps in a 1-T magnetic field

(see sec. 4.6 of ref. [4]). This conventional technology already guarantees a minimum of performance that is highly relevant for  $B$ -physics.

We propose to explore a variation on the time-of-flight method that might yield a factor of 3-4 improvement in the time resolution, and correspondingly a factor of  $\sqrt{3}$ -2 in the momentum range of good  $\pi/K$  separation. For several years now, the best time resolution obtained in a single-photon-sensitive device of several  $\text{cm}^2$  area has been with a microchannel plate photomultiplier (MCP-PMT) [12, 13, 14, 15, 16, 17]. [Small-area avalanche photodiodes have better time resolution [18], but large area devices such as the hybrid-APD [19] appear to have time resolution near 1 ns, limited in part by large device capacitance.] Commercial MCP-PMT's are manufactured in small quantities by Hamamatsu, and the model R3809U, the best version for fast timing, is priced at  $\sim \$11\text{k}$ . Reportedly the cost would be  $\sim \$4\text{k}$  each for an order of 300. MCP-PMT's can also be manufactured with rectangular cross section.

The excellent time resolution and gain of an MCP-PMT are maintained in the presence of strong magnetic fields over a wide range of orientations of the tube, as shown in Fig. 2. They are far superior to ordinary PMT's and even the 'fine-mesh' variations (Hamamatsu R2490U) in this respect.

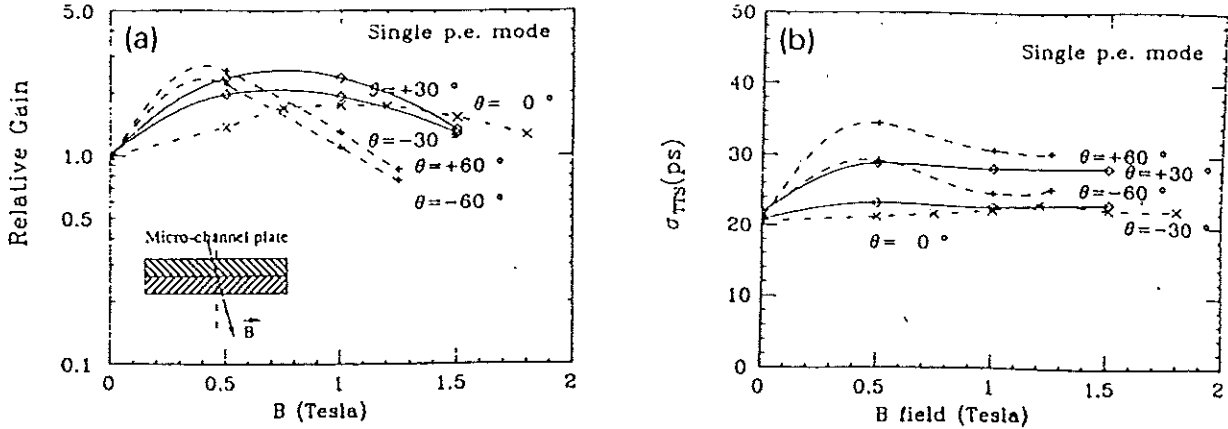


Figure 2: (a) Relative gain and (b) r.m.s. transit-time spread,  $\sigma_{TTS}$ , of a Hamamatsu R2809U MCP-PMT as functions of magnetic-field strength and orientation of the tube axis to the field (from ref. [17]).

The advantage of an MCP-PMT for precision timing is not realized when it is coupled to an organic scintillator with decay time of 1-2 ns [17, 20]; with scintillator bars 5 cm thick, the statistics of the scintillation process limit the time resolution to 100 ps, for which the cheaper fine-mesh PMT's are sufficient.

Instead, one should use the Čerenkov effect, whose inherent time scale is that of atomic orbital motion, *i.e.*, femtoseconds. Recently this option has been advocated by M. Selen [7]. For a time-of-flight system with a modest number of channels for a central detector, the Čerenkov radiation could be produced in a barrel of, say, 128 bars (or fiber bundles) of



length about 3 m with MCP-PMT's on each end. For a barrel of 128 bars at a radius of 1 m the width of a bar should be 5 cm. The thickness of a bar should not be more than about 1.5 cm to keep the r.m.s. transit-time spread due to the extended Čerenkov source to less than 30 ps. A small thickness also is favored to minimize the number of radiation lengths in the bars.

An obvious candidate for the radiator bars is quartz (fused silica), as has also been considered for the DIRC [10, 11]. Fused silica is the only common optical glass with an absorption length significantly longer than one meter, and the only one with good transparency below 350-400 nm.

As noted by Selen [7], the dispersion of optical materials is such that light travels faster at longer wavelengths. Hence the very shortest wavelengths are of less importance for a Čerenkov timing system. For PMT's with a bialkali photocathode the fastest Čerenkov photon rarely has wavelength less than 300 nm. See sec. 2.3.4 for details. Therefore one need not use UV-grade fused silica in this application, resulting in substantial cost savings.

## 2.1 Use of Optical Fiber Hoops as a Delay Line

Selen noted a further advantage of a Čerenkov time-of-flight system for particles of near-normal incidence on the radiator [7]. The difference between the Čerenkov angle for  $\pi$ 's and  $K$ 's results in additional time spread between Čerenkov photons from the two particles when the photons are detected at some distance from the point of emission. That is, the zig-zag path of light inside a radiator of appropriate geometry acts like an optical delay line that enhances the time-of-flight difference for Čerenkov photons from  $\pi$ 's and  $K$ 's. This concept is illustrated in Fig. 3.

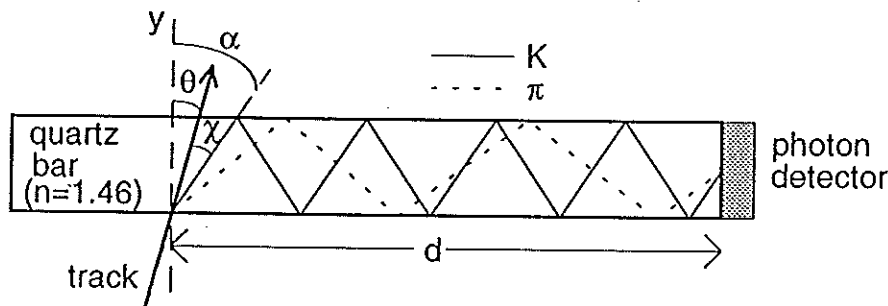


Figure 3: Čerenkov light from  $\pi$ 's and  $K$ 's in a bar or fiber propagates at different angles and hence arrives at the far end at different times. Thus the light guide acts as a delay line to enhance the  $\pi/K$  time-of-flight difference.

To best implement the delay-line scheme in a central detector, the Čerenkov radiators should be arrayed in circular hoops concentric with the beam, as shown in Fig. 4, rather than in a barrel of bars as for a conventional time-of-flight system. In the absence of a magnetic field, particles would pass through the hoops at right angles to the radiator.

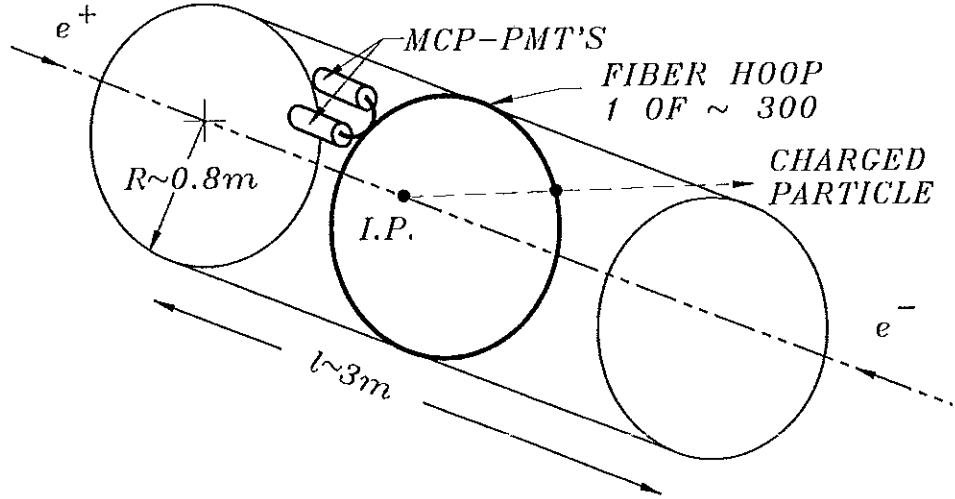


Figure 4: Hoops of quartz fibers form Čerenkov radiators that also serve as optical delay lines.

To illustrate the performance of a fiber-hoop time-of-flight system we consider the decays  $B \rightarrow \pi^+\pi^-$  and  $B \rightarrow \pi^\pm K^\mp$ , which provide the highest momenta  $\pi$ 's and  $K$ 's relevant to  $CP$ -violation measurements. The momentum of such pions is shown as function of laboratory production angle in Fig. 5a for an asymmetric  $e^+e^-$  collider of  $9 \times 3.1$  GeV. In Fig. 5b we show the time-of-flight difference between  $\pi$ 's and  $K$ 's as a function of production angle including both the path of the particles in air and the path of the Čerenkov photons in the fiber hoops. While the time difference in air is as little as 30 ps, if the Čerenkov photons travel at least half way around a hoop of 80-cm radius the time difference is always greater than 130 ps.

### 2.1.1 The Need for Two Layers of Fibers

For an axial magnetic field of 1-1.5 T, the deflection of particles of momenta less than about 3 GeV/c is large enough that Čerenkov light can be captured in the fibers at 80-cm radius only if it is directed in the same azimuthal sense as the particle. That is, the Čerenkov light from a particle propagates down the fiber in only one direction.

To obtain good advantage from the optical delay of the Čerenkov photons, they should travel at least one half the circumference of a hoop. For this, each particle must intercept two hoops for which the ends of the fiber bundles are  $180^\circ$  apart in azimuth.

Then if the MCP-PMT + fiber system delivers a single-photon time resolution of 30 ps or better, we will obtain  $4\text{-}\sigma$  separation of  $\pi$ 's and  $K$ 's over the entire range needed for  $B$  physics. The second layer need not extend beyond a production angle of  $120^\circ$  since time of

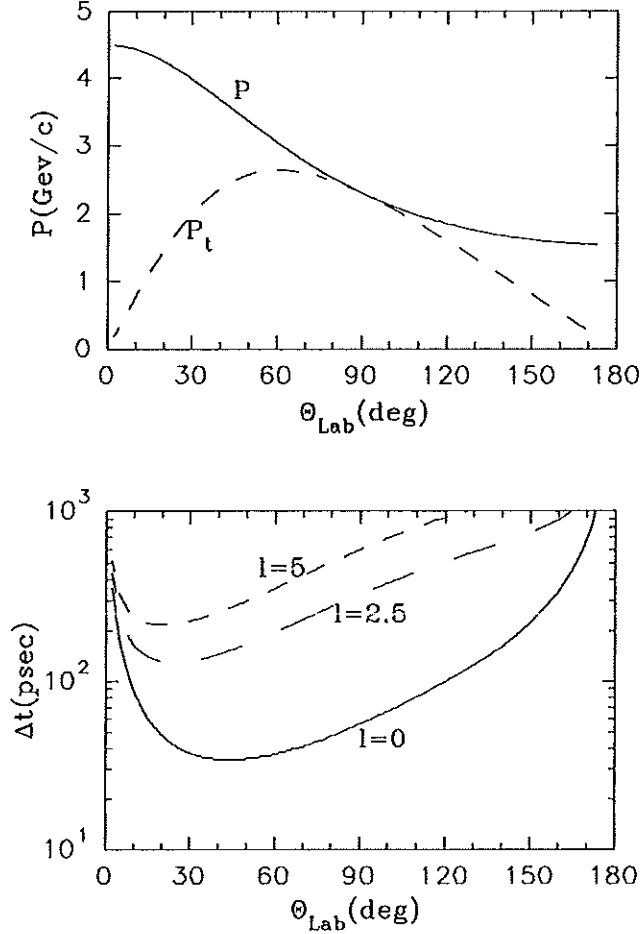


Figure 5: (a) The total momentum and transverse momentum of  $\pi$ 's from the decay  $B \rightarrow \pi^+\pi^-$  as a function of laboratory production angle at an asymmetric  $e^+e^-$  collider with beam energies of 9 and 3.1 GeV. (b) The time-of-flight difference between  $\pi$ 's and  $K$ 's from two-body  $B$  decay. The time difference includes the effect due to the helical path of the charged particles in a 1.2-T magnetic field between the interaction point and the fiber-hoops at radius 0.8 m, as well as the effect of the path of the Čerenkov photons inside the optical fibers. The upper, middle and lower curves are for a 5-, 2.5- and 0-m path in the fibers, respectively.

flight in air suffices for  $\pi/K$  separation at larger angles.

### 2.1.2 Multiple Hits

Since the time-of-flight scheme depends on detection of the earliest Čerenkov photon in a fiber bundle, the system has restricted capability for multiple hits in a bundle. Note that because the light from low-momentum particles travels in only one direction there is a separate multihit problem for positive and negative charges.

If the detector consists of 300 hoops (per layer) and the multiplicity is 6 positive and 6 negative particles the double-hit probability is around 2%. In a two-layer system there is actually a 50% efficiency for two hits (of the same sign) in a hoop due to the 180° azimuthal staggering of the layers.

## 2.2 MCP-PMT Issues

Electron multiplication by secondary emission along a glass microtube was anticipated by Farnsworth in 1930 [21], but first realized in 1961 at Bendix Research Laboratories [22, 24] in both single channel and multichannel configurations. A photomultiplier consisting of a multialkali photocathode coupled to collections of microchannels called Spiraltrons was first demonstrated by Goodrich in 1968 [25], and a commercial MCP-PMT was first manufactured by LEP (France) in 1969 [26]. The Hamamatsu R3809U MCP-PMT is a member of a family based on improvements in the microchannel glass dating from 1983 [27].

Single-channel multipliers are simpler than MCP's, but the large diameter and length of the single channel (required for good rate capability and lifetime) results in poor timing performance.

### 2.2.1 Rate Limitations

Already in 1964 Evans reported [28] that the gain of a microchannel fell off once the count rate exceeded some threshold value. This is interpreted as due to changes in the voltage distribution along a channel when the signal current exceeds about 10% of the standing current. For example, a 'low-resistance' MCP with 10- $\mu$ m channels has  $R \approx 10^7 \Omega$  per  $\text{cm}^2$ , or  $10^{13} \Omega/\text{channel}$ . When operated at 1 kV the standing current is then  $10^{-10} \text{ A/ch} \approx 10^9 \text{ e/ch}$ . Then good performance holds only for signals of up to about  $10^8 \text{ e/ch}$ . If the nominal gain is as high as  $10^6$  there will be gain loss at rates greater than 100 Hz/ch. At a gain of  $10^4$ , as advocated below to increase the device lifetime, there would be good gain stability up to  $10^4 \text{ Hz/ch}$ .

Since a 1- $\text{cm}^2$  MCP has  $\approx 10^6$  channels the total rate capability of the device would be  $10^{10} \text{ Hz}$  at a gain of  $10^4$ . As there would be about 100 Čerenkov photoelectrons per particle traversing a 1  $\text{cm}^2$  fiber bundle, the rate capability would be  $10^8 \text{ Hz}$  per bundle, which seems adequate. At a higher gain of  $10^6$ , however, the rate capability would be only  $10^6 \text{ Hz/ch}$ .

### 2.2.2 MCP Lifetime

In 1965, Smith reported [29] observation of permanent gain loss in MCP's after some fraction of a Coulomb of charge had been collected. For MCP-PMT's there is gain loss both due to damage to the glass walls of the microchannels, and to the photocathode. In both cases the effect is due to positive-ion bombardment. The lifetime of commercial MCP-PMT's appears to be about  $0.1 \text{ C/cm}^2 \approx 10^{18} \text{ e/ch}$  [27]. This lifetime is not adequate for all applications in high-energy physics, and has no doubt discouraged the use of MCP-PMT's in our field.

The lifetime of an MCP-PMT can be increased by nearly an order of magnitude if a layer of Al is deposited over the entrance to the MCP pores to suppress ion motion toward the photocathode. Figure 6 shows data taken by Hamamatsu for one of their R3809U MCP-PMT's with such a coating. The lifetime to one-half gain is about  $1 \mu\text{C/cm}^2$ . However,

there is a penalty in sensitivity for use of the Al layer: the effective quantum efficiency of the tube is reduced by a factor of 0.6.

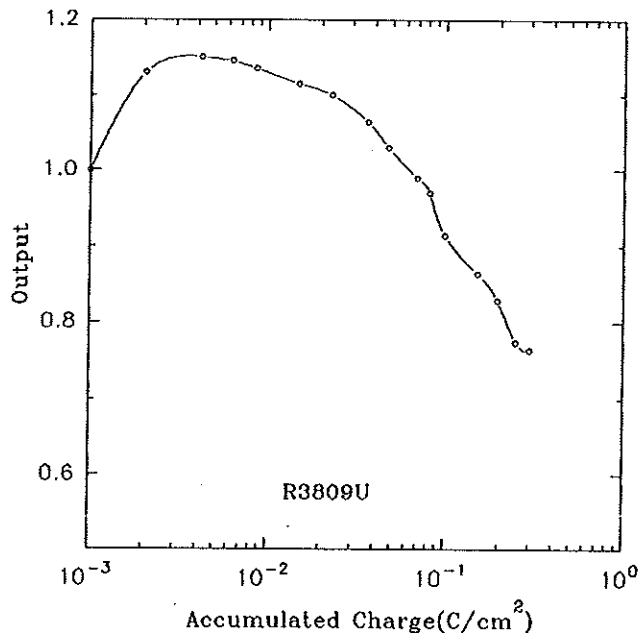


Figure 6: The relative output of a Hamamatsu R3809U MCP-PMT as a function of integrated output charge. This MCP-PMT had an Al coating over the entrance of the MCP to enhance the lifetime.

Clearly the MCP-PMT's will last longer when operated at lower gains. We suggest that the design gain for the time-of-flight system should be  $10^4$ . This will require use of low-noise high-speed amplifiers with each MCP-PMT.

At a gain of  $10^4$  a Čerenkov pulse in a 1-cm<sup>2</sup> fiber bundle yields about  $10^6$   $e^-$ 's, so the MCP-PMT lifetime would be about  $10^{12}$  Čerenkov pulses. For example, at a charged-particle rate of 1 kHz/ch the MCP-PMT life would be 30 years. Since the signal rates at  $e^+e^-$   $B$  factories are less than this the lifetime should be adequate. However, if background rates prove to be higher than 1 kHz/ch, the system is vulnerable.

At a hadron collider where the rates might approach  $10^6$  Hz/ch the use of MCP-PMT's may not be advisable.

Reportedly Galileo Electro-Optics manufactures MCP's with greater lifetime than other vendors. However, it remains to be demonstrated that this advantage holds in an MCP-PMT where lifetime of the photocathode may be the limiting factor.

### 2.2.3 Backgrounds

It was already noted in the original paper on MCP's [22] that they are sensitive to x-rays as well as charged particles. That is, x-ray conversions in the MCP material lead to a potentially serious background at an  $e^+e^-$  collider.

For an MCP of 1-cm<sup>2</sup> area at 1 m from the interaction point, the solid angle is about 10<sup>-5</sup>. Taking the x-ray conversion efficiency to be at most 10%, a flux of 10<sup>10</sup> x-rays/s would lead to a 30-year lifetime. A flux this large would likely be detrimental to the silicon vertex detector and the gas tracking chamber as well.

Also, if the charged-particle background from beam-gas and beam-wall interactions exceeds about 1 MHz into the detector the lifetime will be limited.

Almost certainly the voltage for the MCP-PMT's must be off during filling of the  $e^+e^-$  rings.

We have made estimates of background rates of x-rays and charged particles at an asymmetric  $e^+e^-$  collider as part of a study of rates in a CsI calorimeter [23]. A luminosity of 10<sup>34</sup> cm<sup>-2</sup>sec<sup>-1</sup> was assumed, and the rate of spent positrons was taken to be 2 MHz (large compared to the rate of spent electrons). Charged particles and x-rays from interactions of these spent positrons with beam elements were modelled with GEANT. Bhabha events were generated according to the lowest-order Born cross section. Finally, the rate of synchrotron radiation x-rays above 50 keV into the detector was taken to be 2 GHz.

Figures 7-9 show the calculated rates of charged particles and x-rays from the spent positrons, Bhabhas and synchrotron radiation into the time-of-flight (and fast RICH) system. The total rate of charged particles is predicted to be 250 kHz. Synchrotron radiation is the dominant source of x-rays, but even so the interaction rate of x-rays in the MCP-PMT's is predicted to be less than 100 kHz, summed over all channels. Hence in the estimate the total background rate per channel is about 1 kHz, corresponding to a 30-year system life.

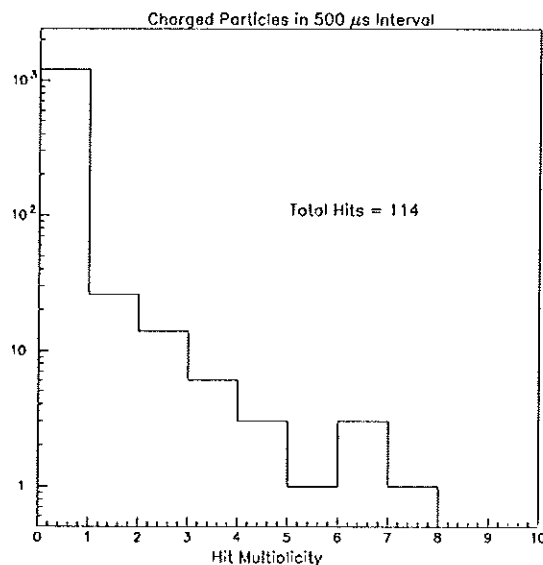


Figure 7: The calculated multiplicity distribution of charged-particles from spent positrons and Bhabhas at an  $e^+e^-$  collider operating at  $\mathcal{L} = 10^{34}$  cm<sup>-2</sup>sec<sup>-1</sup>.

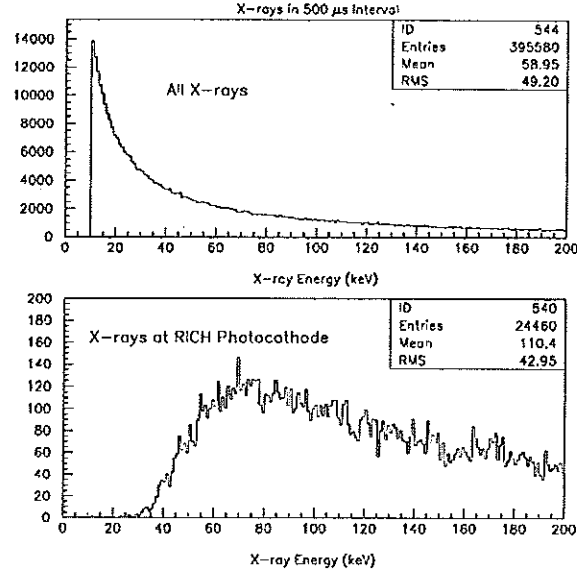


Figure 8: The calculated energy distribution of all x-rays (top) and those reaching the particle ID system (bottom) from spent positrons and Bhabhas at an  $e^+e^-$  collider operating at  $\mathcal{L} = 10^{34} \text{ cm}^{-2}\text{sec}^{-1}$ .

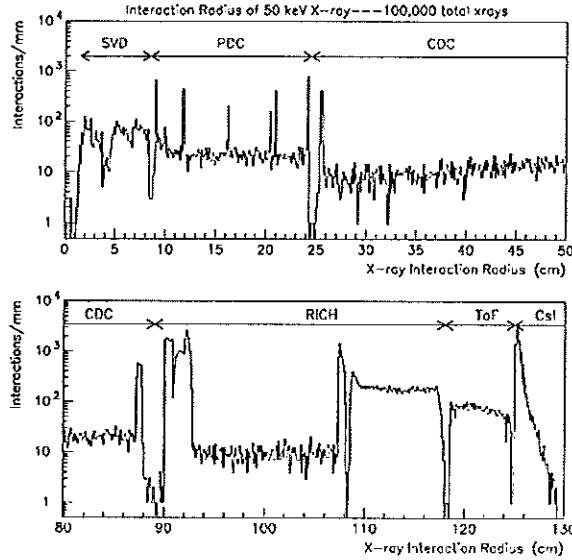


Figure 9: The calculated radial distribution of x-ray interactions from synchrotron radiation at an  $e^+e^-$  collider operating at  $\mathcal{L} = 10^{34} \text{ cm}^{-2}\text{sec}^{-1}$ .

### 2.2.4 MCP-PMT's with Larger Active Area

It appears that the price of an MCP-PMT is only weakly dependent on its active area. MCP's with a useful diameter of 18 mm are readily available as this size is specified for night-vision goggles. A preliminary estimate from Hamamatsu is that a variant of the R3809U with an 18-mm MCP would cost about \$6k in production quantities (plus \$50k for initial development costs), compared to about \$4k for the 11-mm version.

An older Hamamatsu MCP-PMT, model R2809U, achieved a time resolution of 15 ps ( $1\text{-}\sigma$ ) using an 18-mm MCP, so this diameter appears viable for use in the time-of-flight system. Since only 1/3 as many 18-mm tubes would be required, the total cost of such tubes would be about half that for 11-mm tubes.

## 2.3 Fiber Issues

There appears to be no prior use of fibers + MCP-PMT's as a Čerenkov time-of-flight system in high-energy physics. Čerenkov light in fibers has been used as a diagnostic of fiber performance [30] and as a diagnostic of fast-pulse plasmas (*i.e.*, nuclear devices) [31].

Optical fibers preserve the angle of light with respect to the fiber axis, so might appear as candidate radiators for the DIRC option. However, the azimuthal angle of the light is effectively randomized by a long transport, which badly smears the Čerenkov cone compared to the fourfold azimuthal reflection from transport in a rectangular bar.

### 2.3.1 Mechanical Integrity

The proposed fiber-hoop scheme depends on trapping Čerenkov light in a radiator in the form of hoops of radius  $\sim 1$  m. It is not practical to consider solid glass rods bent into hoops due to their fragility. However, the issue of mechanical integrity is critical even for glass fibers.

To capture Čerenkov light from charged particles at near-normal incidence on optical fibers there must be total internal reflection at some boundary. If the fiber core has index  $n_1$  and the index on the far side of the reflecting boundary is  $n_2$  then we must have

$$n_1^2 \geq n_2^2 + 1$$

to capture the Čerenkov light emitted in the core at angle  $\cos^{-1}(1/n_1)$ . For the outer medium being air we need  $n_1 \geq \sqrt{2}$ , which is satisfied by quartz whose index is 1.46.

The core of quartz could be clad by one or more layers, but the needed internal reflection would then take place at the air boundary with the outer cladding layer. As the optical transmission of most cladding layers is far inferior to that of quartz, a typical clad fiber is a poor choice for our applications.

Hence we wish to use quartz as the core and have no cladding. Unclad fibers are not used in commercial applications due to their vulnerability to breaking by growth of microcracks in the presence of water or local stresses (dust particles, abrupt handling, *etc.*).

In principle we could consider fibers with a sapphire core ( $n_1 = 1.68$ ) and Teflon cladding ( $n_2 = 1.3$ ), but the cost of sapphire crystals would be prohibitive.

To explore the feasibility of unclad fibers we have begun discussions with G. Sigel and J. Matthewson of the Rutgers University Fiber Optic Materials Research Program. Their



preliminary comments suggest that unclad silica fibers of 125- $\mu\text{m}$  diameter bent on a 1-m radius could be considered mechanically stable. The bending stress is only about 5 Megapascals compared to the breaking stress of about 700 Megapascals for synthetic silica fiber. The greatest risk of breakage would occur during assembly of the fiber bundles. Long-term survival would be considerably enhanced if the fibers are in a dry-nitrogen atmosphere. It is advisable that the fibers rest on a surface that is a grounded conductor.

Even a 10-cm-radius bend at the ends of the fiber bundles is not excluded. Such a bend would induce a strain of about 100 Megapascals. However, little safety margin remains for handling of the bundle ends during assembly.

A 1-cm<sup>2</sup>-diameter bundle contains about 7000 125- $\mu\text{m}$  fibers. To produce this many 5-m-long fibers in a day the draw rate would need to be  $\sim 1$  m/s. This is in range of industrial capability, but entails rapid handling of the fibers.

Following a discussion with I. Camlibel of Fiberguide Industries we may wish to consider the use of a thin (1- $\mu\text{m}$ ) coating of an organic polymer such as Glassclad 18 (Hüls America). In, say, a 100- $\mu\text{m}$ -diameter fiber with a 1- $\mu\text{m}$ -thick cladding the Čerenkov light would have 2% of its optical path in the cladding. If the attenuation length of the clad is no smaller than 2% of that of quartz this option may be viable.

We are making arrangements to obtain samples of unclad and Glassclad fibers to begin verification of their mechanical and optical performance.

### 2.3.2 Cost

It is too early to have a realistic cost estimate for the fiber bundles, but it will not be less than the cost of the quartz from which the fibers are drawn, which cost is in the vicinity of \$1k per 1-cm<sup>2</sup> bundle.

### 2.3.3 Mechanical Assembly

The fiber bundles must be supported on a low-mass structure with channels to locate the individual bundles. We should consider the use of a carbon-fiber drum of the sort proposed to support straw-tube arrays in one version of the SDC gas tracker.

It appears advisable that the bundles be wound onto the drum directly by the fiber manufacturing to minimize handling.

A major issue is the nature of the coupling of the fiber bundles to the MCP-PMT's. The latter must be aligned along the magnetic field and hence at right angles to the fiber bundles. If, say, 600 PMT's are to be arrayed over the surface of the support drum whose area is about 20 m<sup>2</sup>, each tube + connection must occupy only 0.03 m<sup>2</sup>; for example a region of 20  $\times$  15 cm<sup>2</sup>.

If the fiber bundle is bent on a small radius to make a direct coupling to the PMT, the bend radius must be about 10 cm. This is considerably more stressful than the 1-m bend radius of the hoops and may induce mechanical failures even if the hoops themselves do not.

As an alternative, we will consider the use of short light guides of quartz rod with a 45° mirror. Some loss of light at the mirror would be unavoidable.

The thickness of the array would be about 6 cm, 1 cm for the fiber bundles, 4 cm for the MCP-PMT's, plus 1 cm for the support drum. Cabling of the PMT's would require no

additional thickness as there will be sufficient room between the PMT's for cable paths.

A layer of the fiber-hoop system would constitute about 0.1 of a radiation length ( $= 13$  cm for quartz).

A full-coverage system requires two layers since the Čerenkov light from low-momentum particles travels in only one direction in the fibers and we desire a minimum path of 2.5 m in the fiber.

#### 2.3.4 Dispersion in the Fiber

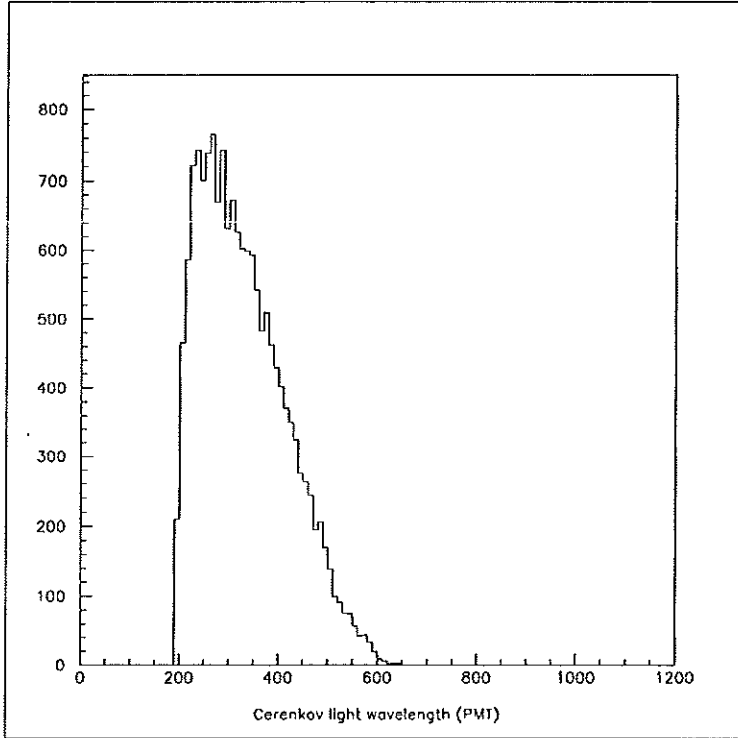


Figure 10: The wavelength spectrum of all Čerenkov photons detected by an MCP-PMT with a bialkali photocathode at the end of a  $1 \times 5 \times 100$  cm<sup>3</sup> quartz bar. The mean number of detected photons is 50.

We have made a simple calculation of the timing accuracy attainable in a 1-m-long quartz bar with cross section  $1 \times 5$  cm<sup>2</sup> using an optical Monte Carlo written by J. Oyang. The simulation includes dispersion and absorption in quartz as well as the quantum efficiency of a bialkali photocathode. Relativistic particles enter the bar normal to a  $5 \times 100$  cm<sup>2</sup> face 1 cm from the end not viewed by the MCP-PMT, and Čerenkov photons are emitted along the 1-cm path in quartz and then tracked until they reach the MCP-PMT or are lost.

Figure 10 shows the wavelength spectrum of all Čerenkov photons detected by the bialkali photocathode of the PMT. There are about 45 photoelectrons per event. Of these only the

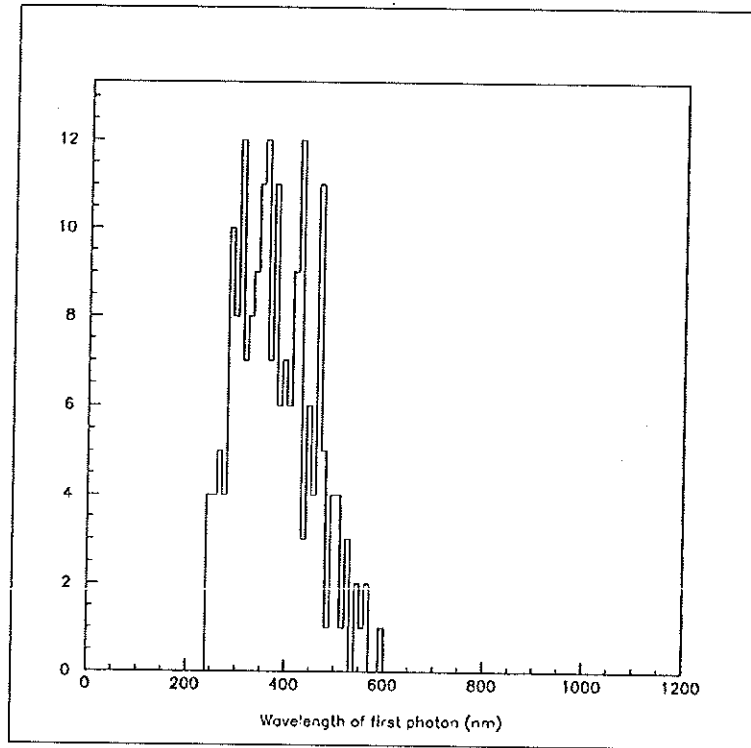


Figure 11: The wavelength spectrum of the earliest Čerenkov photon in each event detected by an MCP-PMT with a bialkali photocathode at the end of a  $1 \times 5 \times 100 \text{ cm}^3$  quartz bar. The spectrum is depleted below 300 nm because the index of refraction is larger at shorter wavelengths.

first is used in the timing measurement. Figure 11 shows the wavelength spectrum of the earliest photon in each event, which has a depletion at short wavelengths as noted by Selen. Figure 12 shows the distribution of optical path lengths of the earliest photon in each event. This distribution has  $\sigma = 20 \text{ ps}$ ; if the MCP-PMT also has intrinsic time resolution of 20 ps (as advertised) then the time resolution of the detector would be 28 ps, *etc.*

### 2.3.5 Čerenkov Light in a Circular Fiber

The total number of Čerenkov photons radiated in a fiber bundle depends only on the path length of the charged particle in the fiber material. However, there is a different efficiency for capture of the Čerenkov light in a circular fiber than in a rectangular bar. We give a preliminary argument that the situation in a circular fiber is favorable.

For the time-of-flight measurement the most important Čerenkov photons are those that propagate quickly down the fiber. These photons lie close to the plane containing the particle's track and parallel to the fiber axis. We claim that a Čerenkov photon lying in this

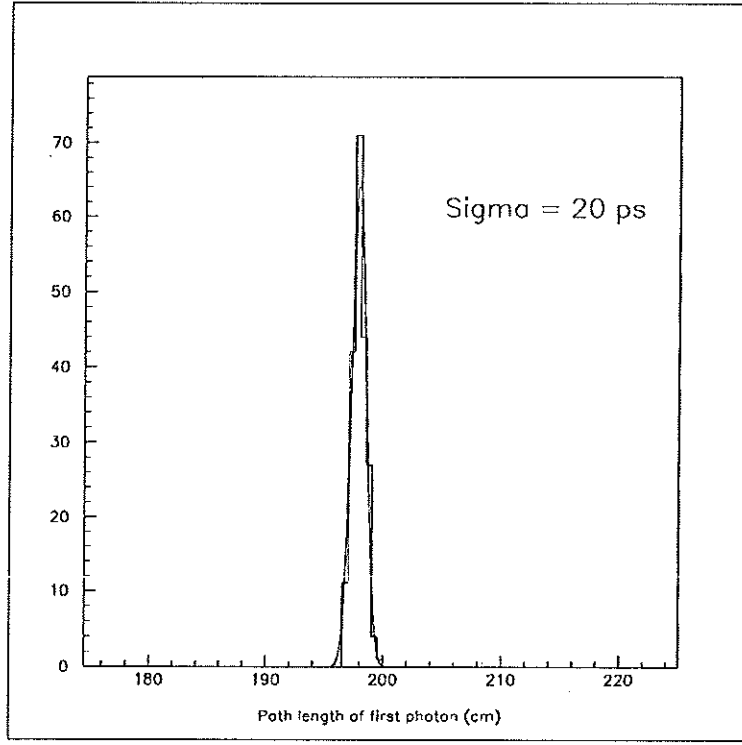


Figure 12: The distribution of optical path lengths of the earliest Čerenkov photon in each event.

plane will be captured for nonzero impact parameter between the track and fiber axis if it would be captured with zero impact parameter.

Consider a particle travelling at  $90^\circ$  to the axis of a fiber, but with some impact parameter  $b < r_{\text{fiber}}$ . Choose coordinate axes with  $z$  along the fiber axis and  $x$  along the particle's track. Then the Čerenkov photon of greatest interest has unit direction vector  $(\cos \theta_C, 0, \sin \theta_C)$  where  $\theta_C$  is the Čerenkov angle.

The normal to the fiber wall at the point where this photon hits is  $(\sqrt{1 - b^2/r^2}, b/r, 0)$ . Hence the angle of incidence,  $\theta_i$ , has  $\cos \theta_i = \cos \theta_C \sqrt{1 - b^2/r^2} \leq \cos \theta_C$ . That is, the angle of incidence inside the fiber is always greater than would be the case for a flat wall perpendicular to the track's direction. Hence the photon is always captured in the fiber if it would have been captured by the wall of a flat bar.

Thus a circular fiber is in no way inferior to a rectangular bar in capturing photons that are likely to travel fast down the fiber.

### 2.3.6 Fluorescence and Radiation Damage

The Čerenkov timing scheme would be defeated by any significant fluorescence (scintillation) in the fibers with a nsec decay constant. Fortunately quartz can be obtained in purities with extremely low fluorescence.

Likewise, quartz is among the most radiation hard of all glassy materials [32], and should show no discernable loss of transparency over a 5-m length for doses up to at least  $10^5$  rad.

The cladding of commercial fibers is more prone to fluorescence and radiation damage than the quartz core. In this respect the use of unclad quartz fibers is an advantage.

## 3 Threshold Čerenkov Counters with Aerogel Radiators and CsI Photocathodes

A Caltech group [33] (see also [5]) has emphasized that a set of threshold Čerenkov counters with radiators of indices 1.008 and 1.06 could provide  $\pi/K$  separation from 0.5 to 4.5 GeV/c, which is well matched to the needs of a central  $B$ -physics detector. No ordinary material has index of refraction of these values, but they can be achieved with silica aerogels. An index as low as 1.008 cannot be achieved by the standard method of aerogel production [34], but it well within range of a process recently developed by Hrubesh *et al.* [9].

A central threshold Čerenkov system at a radius of  $\approx 1$  m would cover about 40 m<sup>2</sup> with 4000 towers of  $10 \times 10$  cm<sup>2</sup> each. With two radiators per tower there are 8000 total Čerenkov cells, each with its own photodetector. A difficulty with this concept is that there is no suitable low-cost photodetector, which must operate in a 1-1.5-T magnetic field. Fine-mesh phototubes and hybrid avalanche photodiodes will cost \$1.5-2k each for devices of only a few cm<sup>2</sup> active area and which must be oriented along the field lines and hence transverse to the general direction of the Čerenkov light.

An interesting option for a photodetector is a CsI photocathode with gas amplification of the photoelectrons. Each Čerenkov cell could have one face covered with such a detector. There would be no optical window, with the aerogel and photodetector in a common gas volume. [A water-free environment is preferred anyway for stability of the aerogel.] By using atmospheric-pressure helium gas with 5% isobutane as the chamber gas we can limit the sensitivity to direct ionization by charged particles to the equivalent of 0.1 photoelectrons [35].

Of course, the simplicity of this concept comes at the price of the restricted range of wavelengths ( $\lambda < 220$  nm) to which CsI is sensitive. Clearly it would be preferable to use a photocathode with sensitivity to longer wavelengths, but all known examples must be processed in vacuum only. Recently V. Peskov has made an interesting effort [36] to fabricate cathodes from CsTe with a TMAE or CsI coating to permit assembly in air, but the results are not yet of sufficient quality.

A critical issue is whether sufficient Čerenkov light with wavelengths below 220 nm reaches the CsI photocathode. Light can be effectively lost both due to absorption and to (elastic) Rayleigh scattering. The latter varies at  $1/\lambda^4$ , so is very severe for wavelengths of interest. The absorption of silica aerogels is not well known for wavelengths near 200 nm, because the Rayleigh scattering is so strong here that a conventional spectrophotometer measures this

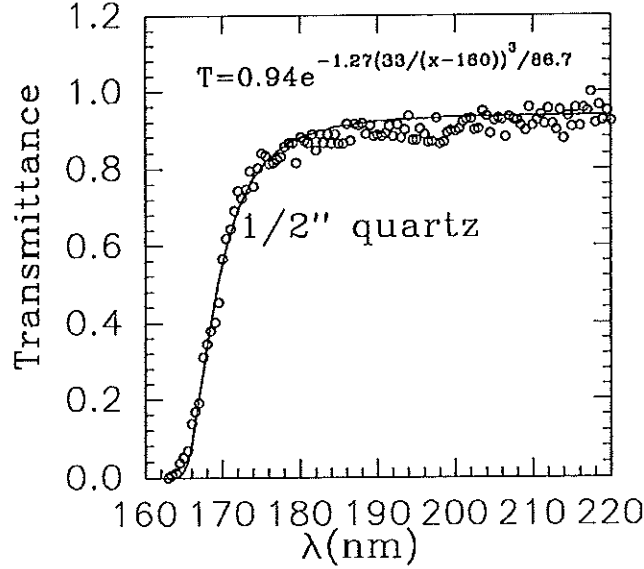


Figure 13: The transmission of UV light through a 1/2''-thick sample of quartz.

rather than absorption.

The amount of Rayleigh scattering appears to depend on the processing history of the aerogel. Recent studies indicate [37] that the new ‘two-step’ aerogels have less Rayleigh scattering than the older type, and that the new aerogels can be improved further by baking at high temperature. For this proposal we use the recently measured values of the Rayleigh scattering length at 500 nm as 3 cm for aerogel of index 1.06 and 10 cm for index 1.008.

We have modelled the performance of an aerogel radiator plus CsI photocathode with an optical Monte Carlo calculation developed by J. Oyang. Čerenkov photons from a line source in the radiator are tracked subject to absorption, Rayleigh scattering and (diffuse) reflection at walls until they reach the CsI photocathode, taken to be rectangular and of the same area as the outer face of the radiator.

In the absence of any direct measurements, we taken the absorption of light in the aerogel to be the same as that for UV-grade quartz (both are made from  $\text{SiO}_2$ ) corrected for the different densities. According to Hrubesh [9], the density of the aerogel is  $0.2(n - 1) \text{ g/cm}^3$ . We have measured the transmission of a 1/2''-thick sample of quartz with results shown in Fig. 13. From a fit to the data, after correcting for losses due to surface reflections, we describe the absorption length by the functional form

$$\lambda_{\text{abs}}[\text{cm}] = 2.4 \times 10^{-3} (\lambda[\text{nm}] - 160)^3,$$

which gives, for example,  $\lambda_{\text{abs}} = 2.4 \text{ cm}$  at 170 nm and 520 cm at 220 nm.

Sample results of the calculation are given in Table 1. If the UV transmission of the aerogels is as good as we assume, it appears that a detector with index 1.06 is very plausible, and one with 1.008 will work albeit with little safety margin. There seems to be only a slight increase in light yield for aerogels of index 1.06 thicker than 2.5 cm and for aerogels of index 1.008 thicker than 10 cm. We consider these calculations to be very encouraging and would

like to proceed to tests of aerogel samples in the near future.

Table 1: Calculated performance of aerogels of index  $n$  and thickness  $t$  coupled to a CsI photocathode with quantum efficiency as shown in Fig. 17. The aerogels have density  $0.2(n - 1)$  g/cm<sup>3</sup>, and UV absorption *vs.* wavelength scaled by density from the expression in the text. The quoted Rayleigh scattering lengths are for 500 nm.  $N_e$  is the mean number of detected photoelectrons.

$n$	$t$ (cm)	$\lambda_{\text{Rayleigh}}$ (cm)	$N_e$
1.06	1	3	10.0
	2.5		23.4
	5		20.8
1.008	15	20	10.2
		10	8.7
		5	5.8
	10	10	7.5
	5	10	4.7

## 4 Fast RICH Detector with CsI Photocathode

Because of the greater amount of information in a reconstructed Čerenkov cone, there can be greater confidence in the identification of particles with a RICH detector than with a time-of-flight system or a threshold Čerenkov counter. Hence we have a strong interest in determining whether proposals for a fast RICH system with CsI photocathode are mature enough for implementation in the coming round of  $B$ -physics experiments.

We have divided our R&D efforts on the fast RICH into 10 topics:

1. We now find good agreement between our measurements of the quantum efficiency of CsI and those of the Breskin group, both of which are in reference to a calibrated NIST photodiode. The value of the Q.E. is intermediate between the ‘high’ and ‘low’ values of recent controversy.
2. We find no temperature dependence to the Q.E. of a fresh photocathode, although transient heating may restore Q.E. lost due to absorption of water vapor.

3. Use of ceramic substrates is advantageous to minimize contamination of the CsI due to outgassing.
4. The possible need for precharging of the CsI photocathode needs further investigation.
5. Aging of CsI photocathodes by photo-ionization of the CsI limits the useful life to fluxes in excess of  $10^{14}/\text{cm}^2$ , which should not be a problem at an  $e^+e^-$  collider.
6. Wire anode planes offer greater protection against sparking than do mesh anodes, but the lower electric field on the cathode leads to some loss of Q.E. in the presence of a chamber gas. Atmospheric-pressure methane is the best choice to minimize the latter problem.
7. A larger anode-cathode gap permits charge-sharing measurements on coarse pads to maintain good spatial resolution while reducing channel count.
8. An analog readout system (*i.e.*, one with ADC's) is preferred.
9. The loss of Čerenkov light for particles with large angles of incidence on a  $\text{C}_6\text{F}_{14}$  radiator could be avoided by tilted radiator modules, at some cost of increased thickness of the detector.
10. Charged-particle and x-ray backgrounds in the RICH detector are not likely to be a serious problem at an  $e^+e^-$  collider.

#### 4.1 Quantum Efficiency of a CsI photocathode

There has been considerable debate in recent months as to the magnitude of the quantum efficiency that can be reproducibly achieved with CsI photocathodes fabricated in modest-quality vacuum systems and subsequently exposed to room air before assembly into a detector. Many measurements, including our own in the past [38], have been made using TMAE gas as the reference for the quantum efficiency. Such measurements can be subject to systematic error due to poor purity of the TMAE, and due to unknown and variable amounts of TMAE adsorbed on chamber windows during the measurements.

To make new measurement of the quantum efficiency of CsI that are not dependent on TMAE we have obtained a calibrated CsTe photodiode from the National Institute of Standards (model 40560C) and also a CsTe photomultiplier (Hamamatsu model R1220) that has been calibrated by the vendor against a similar standard. We have used a VUV monochromator (McPherson model 234/302, shown in Fig. 14) to check the vendor-supplied calibration curves.

First we installed the photodiode (item 7 in Fig. 14) at the front port and the PMT (item 6) at the side port. The VUV beam splitter (item 5) was obtained from Acton Research, who provided calibration curves for its transmission and reflectance within the wavelength range 120-220 nm. A 1-mm diameter collimator (item 9) was placed in front of the beam splitter to restrict the beam spot size. The collecting voltage of the photodiode was set at 150 V. The PMT was operated as a photodiode by connecting all of the dynodes together,



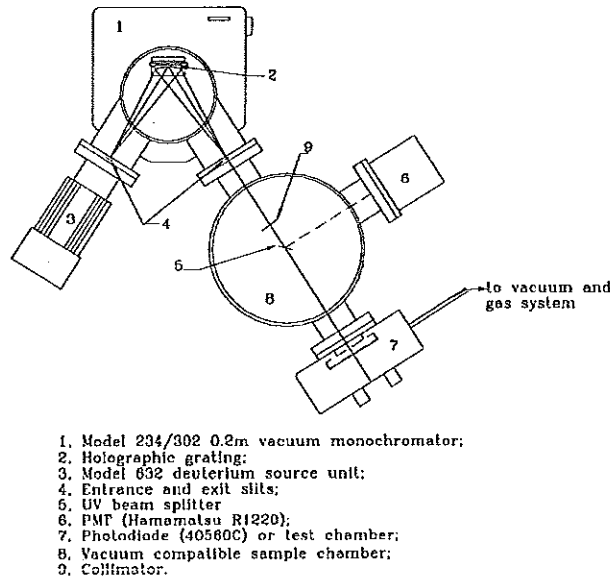


Figure 14: Sketch of the VUV monochromator.

and the dynode voltage set at 120 V. A Keithley model 617 electrometer was used to record the photocurrent. The monochromator was pumped down to less than  $10^{-3}$  Torr to minimize absorption by oxygen. After we scanned both the photodiode and PMT from 120 nm to 220 nm, we swapped photodiode and PMT and scanned again. By this method we checked the consistency of three calibration curves: Q.E. of the photodiode, Q.E. of the PMT, and the ratio of reflectance to transmission of the VUV beam splitter.

We found the stated calibrations of the photodiode and PMT to be consistent to within 10% over the wavelength range 120-220 nm as shown in Fig. 15, except in the region 150-160 nm where  $\sim 25\%$  deviation can be seen. The ratio of reflectance to transmission of the beam splitter shows good agreement with the shape as claimed by the vendor, but the normalization appears systematically shifted by 0.1, as shown in Fig. 16.

Having performed the calibration of photodiode, PMT and beam splitter, we installed the PMT at the side port and an ethane-filled parallel-plate avalanche chamber with a CsI photocathode at the front port. Our new results for the quantum efficiency of a CsI photocathode relative to the calibrated Hamamatsu R1220 photomultiplier are shown in Fig. 17. In the same figure also shown are our previous results which used TMAE as the reference [38]. The new results are somewhat smaller as might be expected. The new corrected data of the Breskin group, measured the the CsI photocathode under vacuum, are also shown [39], and our new results appear to be consistent with theirs. We only show our data above 180 nm because we measured the quantum efficiency in a chamber filled with ethane gas which absorbs UV light for wavelengths shorter than 170 nm [38],

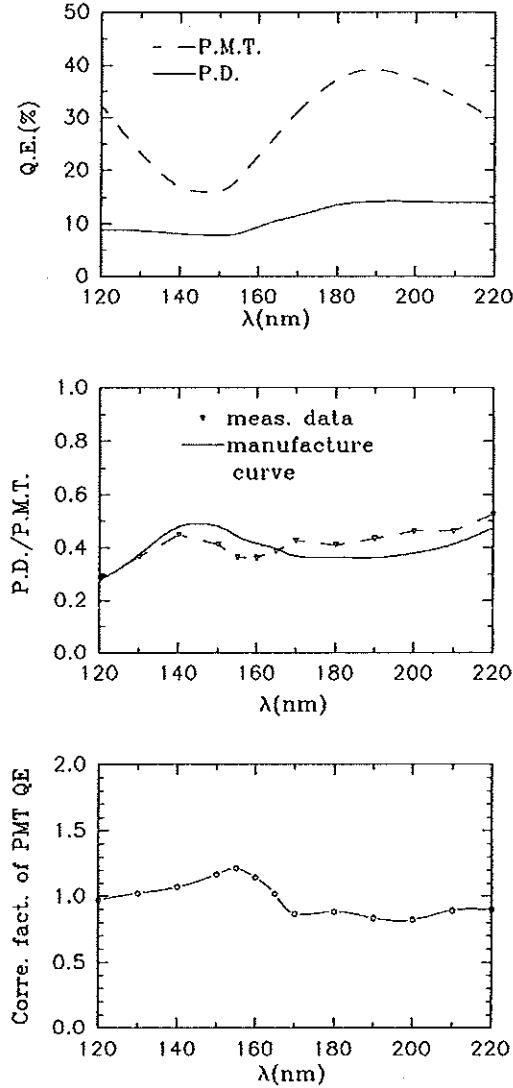


Figure 15: Comparison of the quantum-efficiency calibration of an NIST type 40560C photodiode and a Hamamatsu R1220 photomultiplier. (a) The quantum efficiency *vs.* wavelength of the two devices according to the manufacturers; (b) Measured ratio of quantum efficiencies of the two devices compared to the ratio inferred from manufacturers specifications. (c) Correction factor of PMT Q.E. taking the NIST diode as the reference standard.

It is important to note that our photocathode was exposed to air for a few minutes during assembly of the test chamber, while the photocathodes of the Breskin group were fabricated and tested in the same vacuum system.

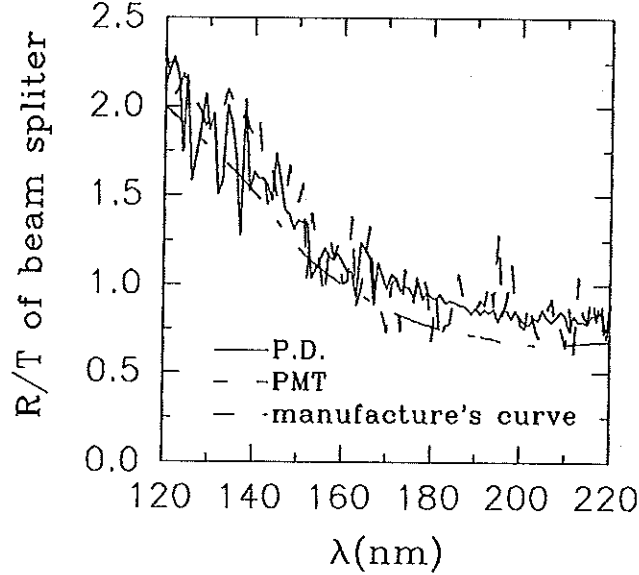


Figure 16: Measurements of the ratio of reflection to transmission of a VUV beam splitter, along with the manufacturer's specification.

## 4.2 Dependence of the Quantum Efficiency on Temperature

There have been conjectures that the quantum efficiency of a solid CsI photocathode might be higher at higher temperatures. The accumulated experience with other semiconductor photocathodes suggests that a strong temperature dependence is unlikely, and at least one null result has been reported for CsI [40].

In contrast to the case of solid CsI, the rapid temperature dependence of the quantum efficiency of TMAE gas is because the vapor pressure of TMAE is higher at higher temperatures [41], so the TMAE density rises and the photoabsorption length falls; the intrinsic quantum efficiency per atom is little affected by temperature.

Recently we have studied the temperature dependence of CsI photocathode under vacuum. A deuterium lamp was the UV light source, followed by two diaphragm collimators to define a beam spot on the test chamber. The beam intensity was monitored by an avalanche photodiode that viewed a fraction of the beam after a beam splitter; the photocurrent was measured by a Keithley 617 electrometer. The experimental procedure was as follows: After installing a freshly made CsI photocathode, we pumped down the test chamber immediately. The beam spot was moved to a certain place on the photocathode and the photocurrent measured at once. Then we shut off the beam and heated the photocathode with an electric heating pad attached on the back side of the aluminum substrate of the photocathode. The temperature was measured by a thermocouple on the top of the heating pad. Once the temperature reached a desired stable value the beam shutter was reopened and the new photocurrent recorded.

The results are shown in Fig. 18 and give no indication of temperature enhancement of the quantum efficiency. If anything, as the temperature increased the quantum efficiency decreased slightly.

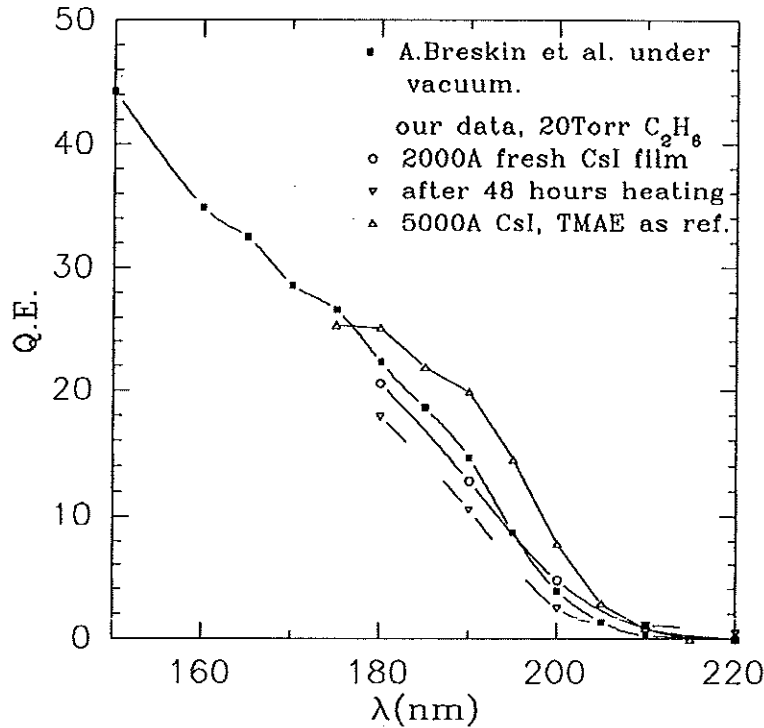


Figure 17: Measured quantum efficiency of CsI photocathodes. Our data (open circles) were collected with the cathode in 20 Torr of ethane, and normalized to the Q.E. of a Hamamatsu R1220 PMT that was calibrated by us against an NIST photodiode. An earlier measurement by us using TMAE gas as a reference [38] is shown as upward triangles. New data from the Breskin group [39] with the CsI under vacuum are shown as boxes. The Q.E. of our photocathode after 48 hours heating at 50°C is shown as downward triangles.

We have also made measurements on a related issue: improvements in the quantum efficiency of CsI photocathodes by transient heating after exposure to water vapor [38]. In such circumstances heating the photocathode can help to get rid of the absorbed water vapor, and to make a full recovery of the quantum efficiency prior to exposure to water (if the humidity exposure is less than 100%).

Any heating of chamber materials surrounding a CsI photocathode carries the risk of driving volatile chemicals onto the photocathode with attendant loss of quantum efficiency. Thus while transient heating of CsI photocathodes can have benefit, care must be exercised in the choice of chamber materials. If the photocathode is prepared with little exposure to water vapor there may be no need for transient heating, as appears to have been the case for our cathode reported in Fig. 17. In that figure we also plotted the quantum efficiency of a fresh made CsI photocathode after being heated for 48 hours while the chamber was being pumped down. The quantum efficiency was lower after heating.

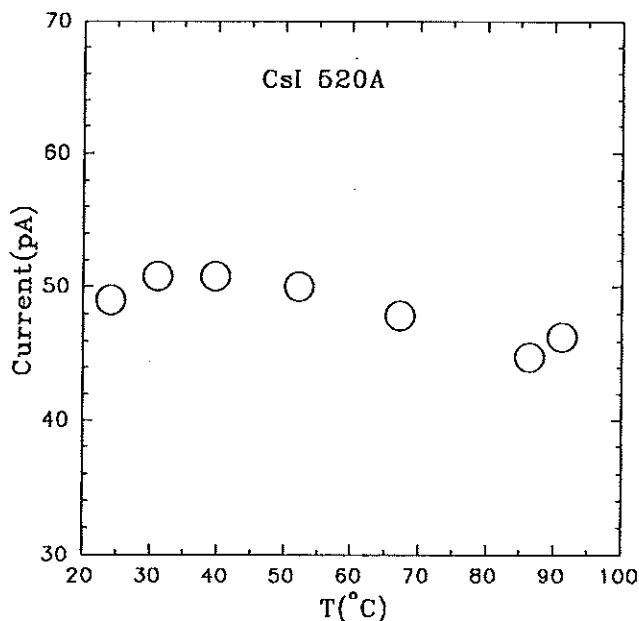


Figure 18: Photocurrent *vs.* temperature for a fresh-made CsI photocathode under vacuum.

### 4.3 Use of Ceramic Substrates

Many of our CsI photocathodes have been deposited onto copper-clad G-10 planes. The G-10 composite is not an ideal material in regards to outgassing, and a ceramic substrate might be superior. In addition, there are reports that CsI can have an adverse chemical reaction with copper substrates [42]. We propose to study CsI photocathodes made on gold-coated ceramic substrates in the near future.

### 4.4 The Need for Precharging of CsI Photocathodes

Various authors have reported a rapid rise in the quantum efficiency of CsI when first exposed to UV light [40, 43, 44]. This could be interpreted as due to the accumulation of a surface charge that aids in the extraction of the photoelectrons. If so, detectors with CsI photocathodes may need to be precharged before use (by UV lamps, perhaps), and possibly after a substantial period of disuse. This issue deserves clarification in the coming months.

### 4.5 Aging of CsI Photocathodes by Charge Transport

CsI photocathodes show a gradual loss of quantum efficiency with increased charge transport [42, 45]. This could be due to a surface effect in response to bombardment by positive ions from the gas avalanche, or due to a bulk effect of ionization of CsI by light. The experimental evidence suggests that this aging is not primarily related to positive ion bombardment, but rather to destruction of the CsI lattice by the photo-ionization. That is, CsI is such a poor

conductor that bulk electrons cannot neutralize a  $\text{CsI}^+$  site before the iodine atom drifts away.

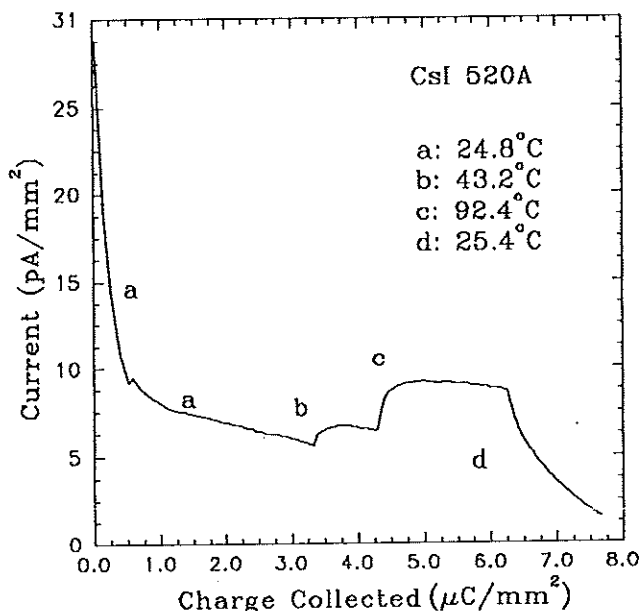


Figure 19: The photocurrent *vs.* total collected charge for a CsI photocathode aged in vacuum. The temperature of the photocathode was varied during the study as indicated.

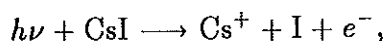
We are currently investigating this issue. A preliminary result is shown in Fig. 19. Two characteristics of the data are worth mention here:

- There is a decrease in quantum efficiency to one half the initial value after accumulation of about  $0.25 \mu\text{C}/\text{mm}^2$ . Beyond an accumulated charge of  $0.5 \mu\text{C}/\text{mm}^2$  the aging rate becomes much slower, with a loss of half the remaining Q.E. after accumulation of about  $5 \mu\text{C}/\text{mm}^2$ .
- For an aged photocathode, some of the lost quantum efficiency can be regained by raising its temperature. In our brief study we found a greater recovery of the quantum efficiency at higher temperature.

To interpret these results we note that one layer of CsI consists of  $\sim 6 \times 10^{12}$  CsI molecules per  $\text{mm}^2$ , while an accumulated charge (at unit gain in vacuum) of  $0.5 \mu\text{C}/\text{mm}^2$  corresponds to  $\sim 3 \times 10^{12}$   $e^-/\text{mm}^2$ . This suggests that the initial decrease of the photocurrent is due to the destruction of the first layer of CsI molecules.

We have measured the photoabsorption length of CsI to be about  $100 \text{ \AA}$  [38], so the number of useful CsI layers is about 20. We infer that the slower aging rate represents the destruction of the deeper layers of CsI.

In photo-ionization of CsI,



we believe that the neutral iodine atoms migrate out of the CsI bulk before the  $\text{Cs}^+$  ions can be neutralized by electrons from the substrate, since CsI is a poor conductor. Hence with time the surface of the CsI photocathode becomes partly Cs. This results in a lower quantum efficiency, but with some sensitivity of photon energies as low as 2 V, the work function of pure Cs. Heating the aged photocathode results in vaporization of the Cs atoms near the surface, so the first 20 or so layers have a higher proportion of CsI and the quantum efficiency rises again.

Anderson *et al.* have reported that the aging of CsI photocathodes is suppressed by the presence of a gain gas in the chamber [45], even when expressing the lifetime in terms of photoelectrons rather than integrated charge. It may be that molecular collisions of the chamber gas with the CsI surface are sufficient to eject the neutral Cs atoms and thus maintain high CsI content of the surface layers.

The useful lifetime of a CsI photocathode is thus at least  $10^{14}$  photoelectrons/cm<sup>2</sup>.

## 4.6 Wire *vs.* Mesh Anodes: Electric-Field Dependence of the Quantum Efficiency

The motivations for use of anode wire planes instead of anode mesh planes are several:

- Chambers with wire anodes will be able to operate at atmospheric pressure with pure organic gases such as methane, ethane and isobutane. A parallel-plate avalanche chamber (PPAC) with a mesh anode can operate only at low pressure with these gases. A PPAC can operate with atmospheric-pressure helium gas mixtures, but the penalty is lower quantum efficiency of the photocathode due to scattering of photoelectrons back onto the cathode [35].
- According to the in-beam experience of the CERES UV-detectors [46] a PPAC configuration is more vulnerable to the sparking due to the fast breakdown occurring at a total charge of  $10^8$  e's in an avalanche. Such large avalanches are due to nuclear interactions near the surface of chamber materials. In an anode-wire configuration the avalanche size is self-suppressed because of space-charge effects if the avalanche is larger than  $10^6$  e's, and the probability of sparking is greatly reduced.

Several works have suggested the quantum efficiency of photocathode depends on the electric field at the surface of the photocathode [44, 49]. Since the electric field at the cathode plane is quite different for PPAC and MWPC, we want to understand how much the quantum efficiency will be influenced by the chamber configuration.

We have made recent studies for this purpose with an anode wire plane and a cathode mesh plane added to a small RICH prototype that was previously used in tests at BNL [47]. A sketch of the chamber is shown in Fig 20.

After an anode wire plane and a cathode mesh plane were installed in the prototype chamber, we operated it with atmospheric methane, ethane and isobutane. Typical gas-gain spectra of single-photoelectron-initiated gas avalanches, together with the gas gain *vs.* high voltage, are shown in Fig. 21. The single-pad gain shown in Fig. 21 should be multiplied by a factor of 2.74 to obtain the total gain; this includes a factor of 2 since there are two

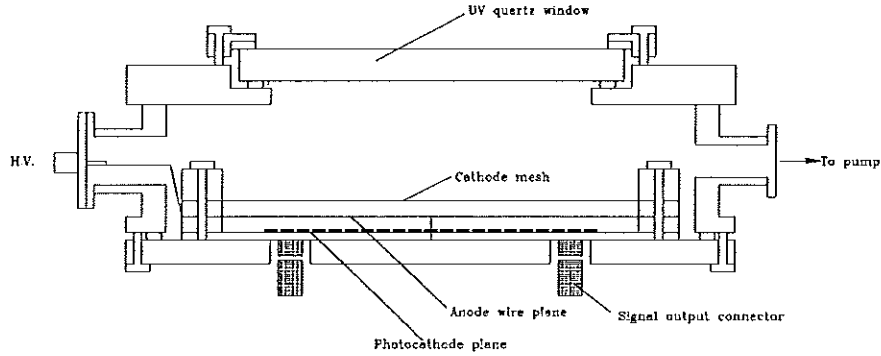


Figure 20: A RICH prototype with an anode-wire plane.

cathode planes, and a factor of 1.37 as the ratio of the charge on one plane to the charge induced on the central pad.

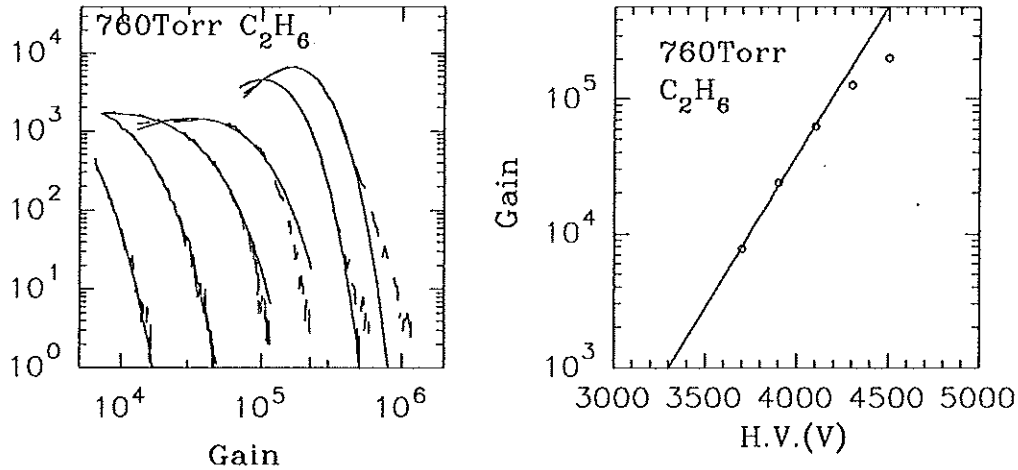


Figure 21: Induced-charge spectra on one central cathode pad in a RICH prototype with MWPC configuration. (a) Charge spectra; (b) Gain vs. high voltage.

In Fig. 21b we show the results for ethane gas; methane and isobutane have similar behaviours. For six different pressure of ethane gas (760, 376, 200, 94, 49, and 20 Torr) the charge spectra were collected. Because the shapes of those spectra are different the threshold effects are different. To compensate the lost part of the spectra below the threshold each spectrum is fitted a Polya distribution, and the number of events below the threshold of



fitted Polya curve are added to the integral of the observed spectrum to get a total quantum efficiency.

The electric field at the cathode can be calculated from Ref. [48]:

$$E_y \simeq \frac{2\pi V_0}{2\pi d/s - 2\ln(\pi D/s)}, \quad d > s,$$

where  $E_y$  is the electric field along with the  $y$ -direction, which is perpendicular to the anode wire plane,  $d$  is the distance between anode and cathode planes,  $s$  is the anode wire pitch,  $D$  is the anode wire diameter, and  $V_0$  is the high voltage on the anode wire.

The relative quantum efficiency *vs.* the reduced electric field ( $E/P$ ) at the photocathode is shown in Fig. 22. We observed a 20% reduction of quantum efficiency at 760 Torr compared to that at low pressure (high reduced electric field).

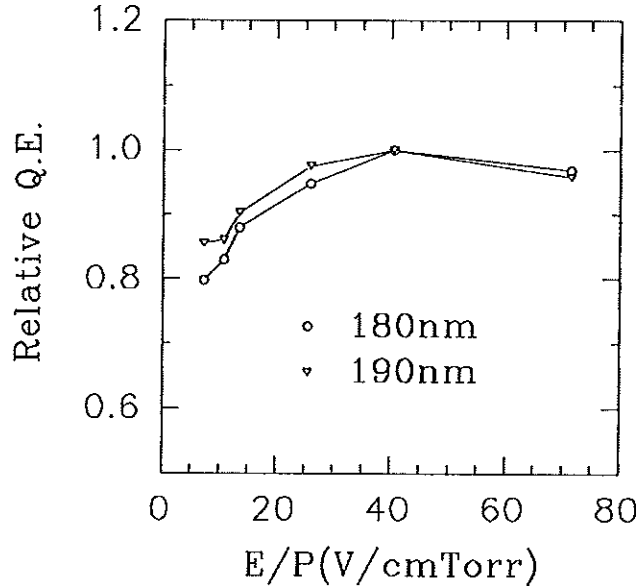


Figure 22: The dependence of the quantum efficiency on the reduced electric field,  $E/P$ . The six values of  $E/P$  correspond to pressure of ethane gas of 760, 376, 200, 94, 49, and 20 Torr, from left to right.

This result contrasts with that for CsI under vacuum, where H. Bräuning *et al.* found no (or very little) electric-field dependence of the quantum efficiency over the range of 50-2000 V/mm [40]. This null result is expected since the mean free path length photoelectrons in solid CsI is only a few nm. Hence for any influence on the electron extraction from the CsI, the electric field should be around 1 V/nm, which is several orders of magnitude higher than the applied electric fields of  $\sim 1$  kV/mm.

Our results on electric-field effects on the quantum efficiency of CsI photocathodes in gas media are quite consistent with those of the Breskin group [49] who found a Q.E. reduction in gases of about 3% for methane,  $\sim 20\%$  for ethane, and  $\sim 30\%$  for isobutane, compared to vacuum. We concur with their conclusion the Q.E. of a CsI surface in gas is always lower

than in vacuum due to the backscattering of photoelectrons from gas molecules. For high values of the reduced electric field the gas avalanche starts close to the photocathode, so the probability for elastic scattering decreases due to the opening of new inelastic channels in the electron- molecule collisions. When the probability of the elastic collisions drops to zero, the Q.E. in the gases must reach the vacuum value.

We have measured the reduced Townsend coefficient  $\alpha/P$  of ethane and isobutane [35]. From fits to the data of the form  $\alpha/P = a + bE/P$ , we derived the minimum reduced electric field required to start the gas avalanche,  $(E/P)_{\min}$ , which is 56.1 V/cm-Torr for ethane, and 89.9 V/cm-Torr for isobutane. Such high reduced electric fields at the cathode only can be reached under low gas pressure.

## 4.7 Charge Sharing on the Cathode Readout Pads

The reconstruction of Čerenkov rings in RICH detectors with dimensions appropriate for central  $B$  physics requires spatial resolution of about 3 mm. Finer resolution is not warranted because of limitations of chromatic aberration in the radiator, and because of broadening of the ring due to the finite thickness of the radiator in the case of proximity focusing. This has led to a specification of readout pad size of typically  $8 \times 8$  mm, and correspondingly a channel count of about 600k for a detector of  $40 \text{ m}^2$  surface area.

If the anode-cathode spacing is increased, the image charge on the cathode pads will be smeared over multiple pads and good spatial resolution could be obtained by charge sharing among coarser pads [50]. The spatial distribution  $\rho(x)$  of the image charge is governed by the chamber gap, called  $d$  in Fig. 23, according to [51]

$$\rho(x) = \frac{\pi}{8} \text{sech}^2 \left( \frac{\pi x}{2d} \right).$$

The magnitude of the image-charge distribution depends on the size of the gas avalanche for a single photoelectron, which is well modelled by the Polya distribution [52]

$$P(a) \propto a^{b-1} e^{-ba},$$

where  $a \equiv G/\bar{G}$ ,  $G$  being the gain for a particular electron and  $\bar{G}$  being the mean gain, and  $b$  is related to the width of the distribution by  $(\sigma_a/a)^2 = 1/b$ . Setting  $b = 3/2$  gives a reasonable description of the gain spectrum in typical chamber gases, as shown in Fig. 24. From the figure we also see that the electronics threshold must be less than  $0.1\bar{G}$  to maintain 95% detection efficiency.

The reconstructed location of a photoelectron is obtained by simple charge weighting of the struck-pad coordinates. From the spatial distribution of the image charge we can calculate the relation between true and reconstructed position as in Fig. 25. Furthermore, we can estimate the fluctuations in reconstructed position due to fluctuations in gain as

$$\sigma_x = \frac{\sigma_Q}{Q} F(d/w),$$

where  $Q$  is the total charge observed,  $\sigma_Q$  is the electronics noise, and  $F$  is an auxiliary function shown in Fig. 26 pertaining to the use of the curves of true *vs.* reconstructed position [50]. We

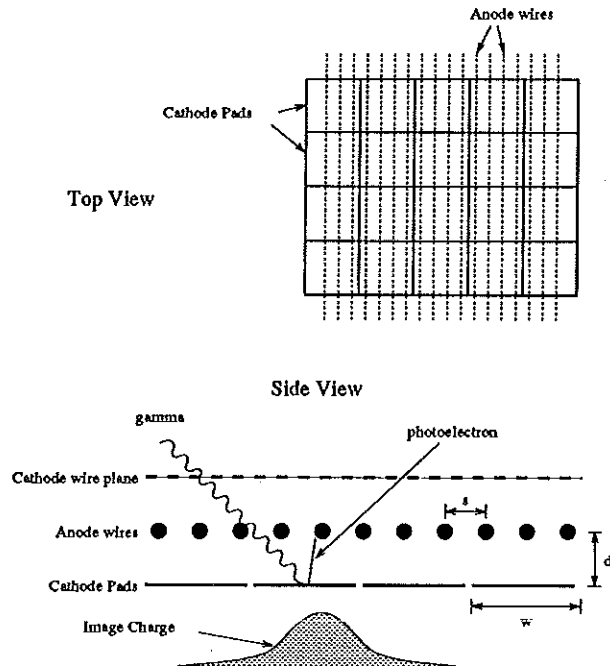


Figure 23: Design of a RICH photodetector with a CsI photocathode segmented into pads of width  $w$  separated by a gap  $d$  from the anode plane consisting of wires of spacing  $s$ .

see that when using information only from a  $3 \times 3$  array of pads the optimum gap thickness is  $d = 0.7w$ , although there is little penalty to reducing the gap to  $0.5w$ . The final result can be summarized as

$$\frac{\sigma_x}{w} = \frac{140\sigma_Q}{\bar{G}}.$$

For example, with pad width  $w = 16$  mm, noise charge  $\sigma_Q = 2000$   $e$  and mean gain  $\bar{G} = 2.5 \times 10^5$  we expect spatial resolution of 2 mm, which is adequate.

Hence we propose increasing the chamber gap to 8 mm from the present typical value of 1.6 mm and increasing the pad size to  $16 \times 16$  mm<sup>2</sup> to deliver the desired spatial resolution while reducing the pad count by a factor of 4. Of course, the readout electronics must include digitization of the pulse height to achieve this reduction. The use of a thicker chamber gap will provide an analog storage time for the Čerenkov signal of order 1  $\mu$ s, which is well matched to the signal-processing strategy at an  $e^+e^-$   $B$  factory.

To test the charge-sharing idea, we have installed the RICH prototype (Fig. 20) vertically on a  $x$ - $y$  stage. The entrance window of RICH prototype touched the exit window of the UV monochromator (Fig. 14). Three consecutive horizontal pads of dimension  $8 \times 8$  mm<sup>2</sup> were connected together to form a “pseudostrip”, the induced charge on which was measured with an EG&G ORTEC 142PC preamplifier for several vertical positions of the UV beam with results shown in Fig. 27. The data match the theoretical curve very well (after a small correction for the use of a 24-mm-long strip rather than an infinite strip).

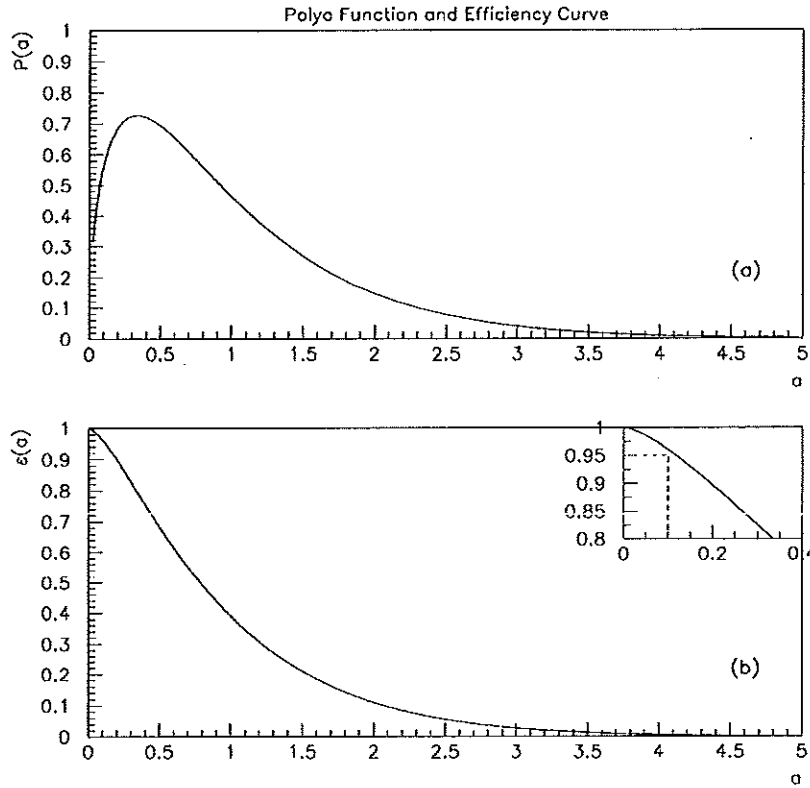


Figure 24: (a) The Polya distribution of gain of a single-electron avalanche as a function of relative gain  $a = G/\bar{G}$  for parameter  $b = 3/2$ . (b) Detection efficiency as a function of an electronics threshold at relative gain  $a$ .

## 4.8 Analog *vs.* Digital Readout

As a fast RICH system will have of order  $10^5$  channels it is natural to consider simple (digital) readout electronics that only indicates the presence or absence of a signal above threshold in each channel. Nonetheless we are pursuing implementation of (analog) readout electronics with an ADC for every 256 channels. An analog system is desirable and plausible for a number of reasons:

1. The required electronics can be fabricated as a custom ASIC that is conservative by present standards.
2. A low-noise charge-sensitive preamp permits operation of the RICH chambers at low gain.

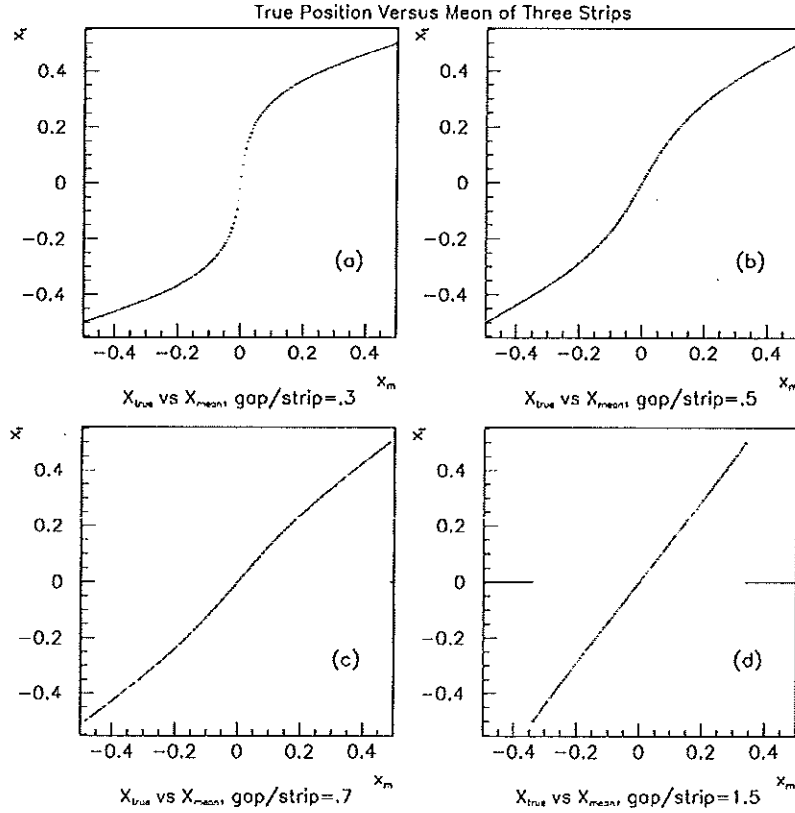


Figure 25: A model calculation of true *vs.* reconstructed position of photons detected in a pad chamber for various values of the ratio  $d/w$  of gap thickness to pad width.

3. The necessary integration time ( $\sim 2\mu\text{s}$ ) for good pulse-height resolution acts as an analog storage of the RICH signals.
4. Improved spatial resolution via measurement of charge sharing permits a lower channel count.
5. Minimum-ionizing particles are identified by pulse height.
6. A design with individual channel thresholds permits disabling of bad channels.
7. Pulse-height information provides good diagnostics of chamber performance.
8. A simple architecture with relatively few interconnects can be used.

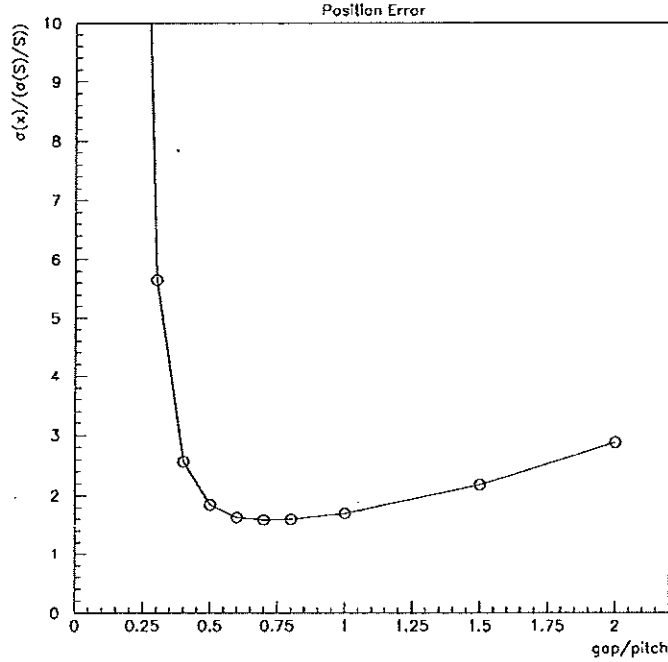


Figure 26: A model calculation of error in the reconstructed position of photons detected in a pad chamber for various values of the ratio  $d/w$  of gap thickness to pad width. Only a  $3 \times 3$  array of pads is used in the analysis, which leads to the rise in error for large  $d/w$ , where the image charge is distributed over a larger area. The error is normalized to the relative error in the charge measurement.

9. Power consumption will be only  $\sim 1$  mW/channel.
10. The electronics on the detector have low mass and low profile.
11. The cost per channel is only slightly higher than for digital electronics.

Figure 28 shows a conceptual design of the mounting of the readout chips, one per 64 detector channels. Figure 29 sketches a block diagram of the front-end electronics, which is similar in concept to that of many silicon-vertex-detector readout systems. The integrate-and-hold with a  $2\text{-}\mu\text{s}$  peaking time provides a trigger delay. Candidate readout chips for asynchronous operation include AMPLEX and VIKING.

We are presently preparing a 64-channel prototype readout with AMPLEX chips to be used with the small test RICH detector described in previous sections.

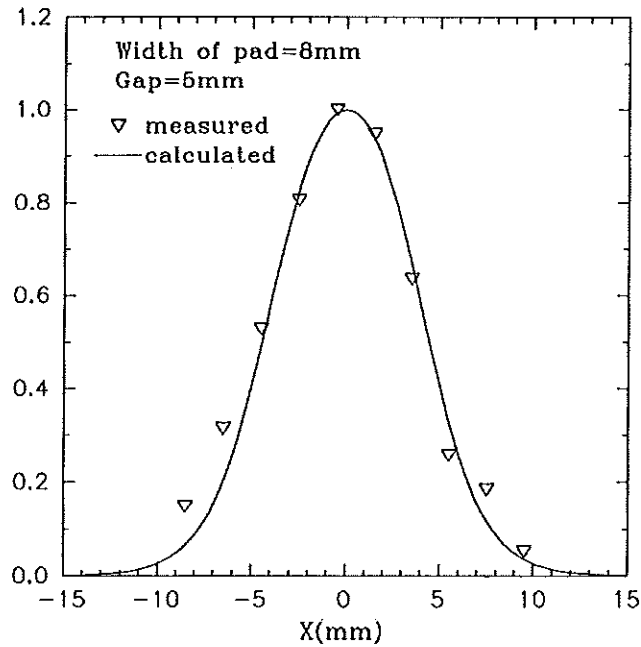


Figure 27: The distribution of induced charge on an 8-mm-wide "pseudostrip" vs. the distance from its centerline to the gas avalanche.

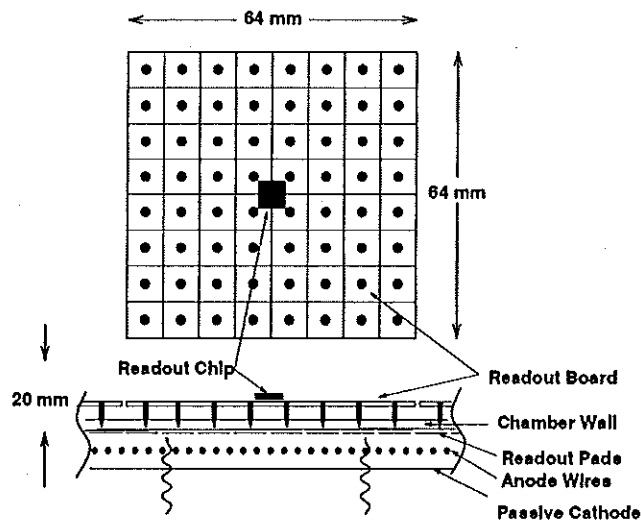


Figure 28: A sketch of the mechanical layout of the RICH front-end electronics.

Figure 30 sketches the concept of the off-detector data acquisition system. The system would reside in VME (or FASTBUS) crates with 64 DAQ channels per board, each channel scanning 256 detector pads. The system would include an individual thresholds for each channel, pedestal subtraction, zero suppression and bad-channel disable. The scanning rate would be 2 MHz.

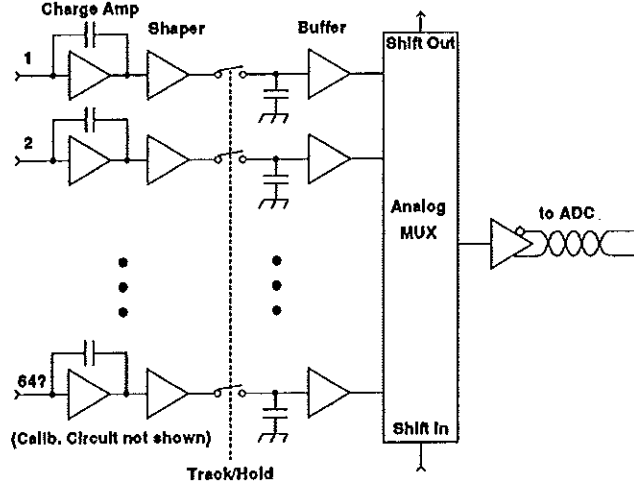


Figure 29: A block diagram of the RICH front-end electronics.

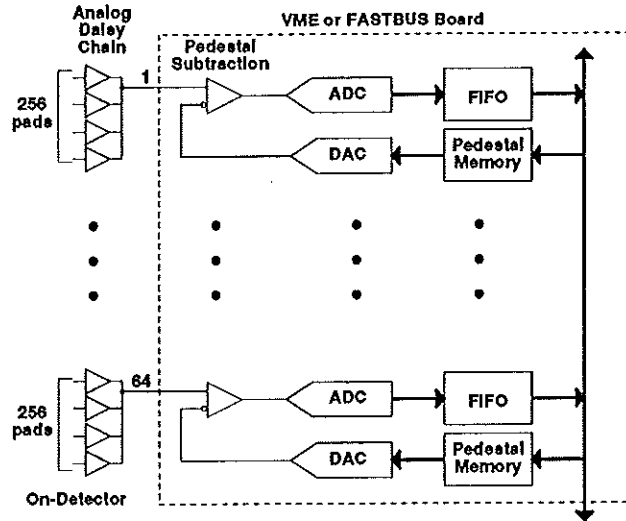


Figure 30: A block diagram of the RICH off-detector data acquisition system.

Engineering design of the off-detector DAQ system is underway.

## 4.9 Tilted RICH Modules

In many designs of barrel RICH detectors the  $C_6F_{14}$  radiator modules are parallel to the beam axis. This has the unfortunate consequence that only part of the Čerenkov cone emerges from the radiator for particles of non-normal incidence. We are considering the merits of dividing the RICH detector into modules with the radiator more nearly normal to the incident particles.

For a radiator of index  $n$  ( $= 1.27$  for  $C_6F_{14}$ ) the Čerenkov angle is  $\theta_C = \cos^{-1} 1/n$  ( $=$



$38^\circ$  for  $C_6F_{14}$ ) and the Čerenkov light is internally reflected at the radiator surface if the angle of incidence of the light is greater than  $\theta_{\text{int}} = \sin^{-1} 1/n (= 52^\circ \text{ for } C_6F_{14})$ . Hence some of the Čerenkov cone is internally reflected if the particle has angle of incidence  $\theta_i$  greater than  $\theta_{\text{int}} - \theta_C (= 14^\circ \text{ for } C_6F_{14})$ . Indeed, light with azimuth  $\phi$  with respect to the particle's direction is internally reflected for all  $\phi$  less than that given by

$$\cos \theta_{\text{int}} = \cos \theta_i \cos \theta_C + \sin \theta_i \sin \theta_C \cos \phi.$$

For example, 50% of the Čerenkov light is internally reflected for  $\theta_i = 39^\circ$  for  $C_6F_{14}$ .

In a barrel RICH detector for a  $B$  factory, angles of incidence up to  $60^\circ$  are contemplated. The attendant loss of light due to internal reflection renders the performance of the detector very marginal at such large angles of incidence. Furthermore, because the 'rings' detected at large angles of incidence have hits over only part of the azimuth the origin of the 'ring' must be provided by the tracking detector. The required spatial accuracy on the intercept of the track with the radiator for good  $\pi/K$  separation is less than a millimeter, which puts severe demands on the  $z$ -measurement in the central tracking system.

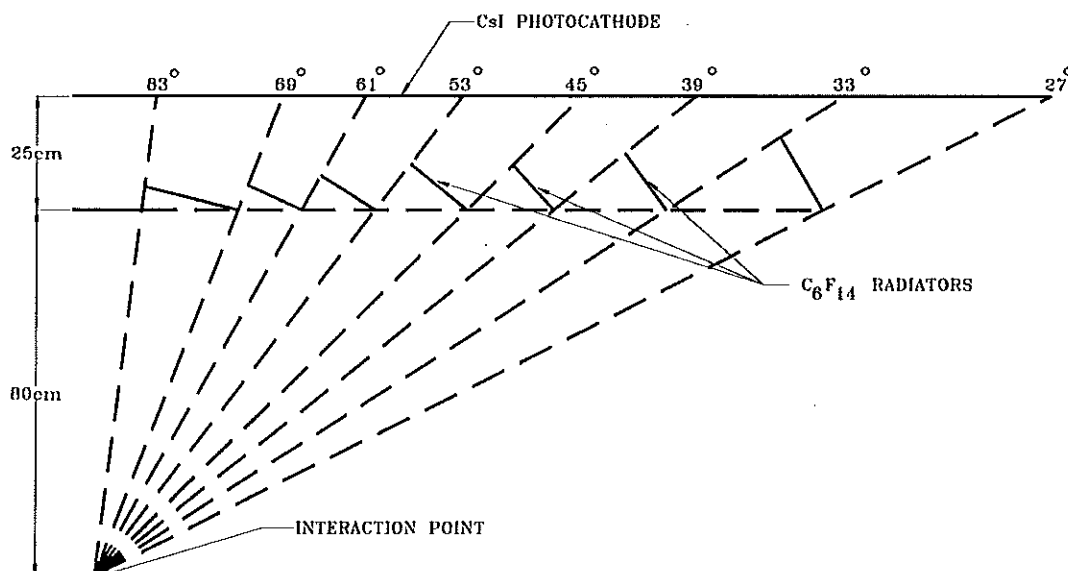


Figure 31: A sketch of the mechanical layout of a barrel RICH detector with tilted radiator modules such that all Čerenkov photons escape from the radiators.

Hence it may be preferable to have a RICH detector design with radiator modules such that the angle of incidence never exceeds  $15^\circ$ . The radiator modules would then be projective, as sketched in Fig. 31. The modules would consist of liquid  $C_6F_{14}$  sealed in quartz containers with two optical windows. A front optical window is required so the Čerenkov light from the near edge of an adjacent radiator at larger angles can still reach the CsI photocathode.

The CsI photocathode could remain on the surface of the outer barrel of the RICH detector, permitting the anode to be made from long wires parallel to the beam axis. However,

if it is desired that the drift space normal to the radiator be, say, 20 cm, then the outer radius of the RICH detector must be about 25 cm larger than the inner radius. That is, the improved performance of the RICH detector at small production angles comes at the expense of greater radial thickness.

#### 4.10 Backgrounds

The background study reported in sec. 2.2.3 applies to a RICH detector as well. For a luminosity of  $10^{34}$  we estimate a background charged-particle rate in the detector of 250 kHz, and about 2 MHz of conversions of synchrotron-radiation x-rays in the CsI. Such backgrounds present little problem for the RICH detector due to the channel count of order  $10^5$ .

## 5 R&D Proposal

### 5.1 R&D Goals

#### 5.1.1 Time-of-Flight System

We propose to demonstrate a high-resolution time-of-flight system based on multichannel-plate photomultipliers (MCP-PMT's) that view Čerenkov light produced in silica fiber bundles. Steps in the proposed R&D include:

1. Procurement of two Hamamatsu R3809U MCP-PMT's at  $\sim$  \$11k each. This is the critical-path item.
2. Verification of the intrinsic time response of the MCP-PMT's with a picosecond laser system (available at Princeton U.).
3. Procurement of sample silica fibers, both unclad and with very thin cladding (\$5k).
4. Optical and mechanical characterization of the fiber samples.
5. Measurement of the time resolution of the MCP-PMT + radiator system using cosmic rays and/or a test beam.
6. Submission of a Request for Quotation for custom MCP-PMT's to vendors including Hamamatsu, SAIC, Ball Aerospace, Philips, *etc.*

#### 5.1.2 Aerogel + CsI Threshold Čerenkov Counters

We propose to study whether the 'two-step' aerogels produced by Hrubesh *et al.* of LLNL has sufficient UV transparency to be matched to CsI photocathodes to form low-cost threshold Čerenkov counters. Steps in the proposed R&D include:

1. Procurement of samples of 'two-step' aerogel with indices 1.06 and 1.008 from the LLNL group. These samples should be prepared for maximum UV transparency. This is the critical-path item.

To facilitate later characterization of these samples some or all of them should be prepared in  $10 \times 20 \times 45$  mm<sup>3</sup> fluorimetry cells made from UV-grade fused silica (NSG type 3-ES-20 or equivalent, \$150 ea.).

Samples made using high-temperature solvent extraction should be baked further; it is not yet determined whether this baking should be performed at Princeton or elsewhere.

We would like to obtain some aerogel samples prepared via solvent extraction by low-temperature CO<sub>2</sub> substitution. Such samples are hygroscopic so some care is required in their handling.

2. Measurement of the UV-transparency (and Rayleigh scattering length) of the aerogel samples in our vacuum spectrophotometer. In an attempt to separate Rayleigh scattering from absorption we will surround most of the sample cells with high-reflectivity wrapping.

3. Following successful characterization of the first samples we would then construct prototype threshold counters incorporating aerogel and a CsI photocathode in a common volume of He/isobutane 95/5. For this the aerogel samples should be roughly  $10 \times 10 \times 2.5 \text{ cm}^3$  for index 1.06, and  $10 \times 10 \times 10 \text{ cm}^2$  for index 1.008.

The prototype modules would be tested with cosmic rays and/or a test beam.

### 5.1.3 RICH Detector with CsI Photocathode

We propose to continue our ongoing R&D into this technology, using existing funding for steps 1-6 listed below:

1. Modify the existing 8"-diameter prototype chamber to operate with larger pads and a larger gap.
2. Build a wire anode plane to replace the existing wire-mesh plane.
3. Replace the 432 channels of SVX electronics for the pad readout with a readout based on CERN Amplex chips that is capable of asynchronous operation.
4. Compare the use of G-10 and ceramic as the material for dielectric components of the chamber.
5. Test the modified prototype with our vacuum spectrometer, followed by beam tests at TRIUMF. These tests will be performed with both atmospheric- and low-pressure chamber gas.
6. Continue studies of turn-on-transient and aging effects in separate small test chambers.
7. Initiate a program of construction of larger prototype chambers of area  $\sim 50 \times 50 \text{ cm}^2$ . This will require a new evaporator and oil-free vacuum system ( $\sim \$25\text{k}$  even with used components other than the vacuum pumps)

## 5.2 Personnel

This R&D will be performed by the authors of this note, with K. McDonald as the contact person. The proposed R&D is the primary physics effort of C. Lu, D. Marlow and graduate student Z. Cheng, and is 50% of the research effort of K. McDonald and E. Prebys.

We benefit from an ongoing collaboration on R&D into RICH detectors with CsI photocathodes with physicists from U. Penn (N. Lockyer, spokesperson).

The Princeton U. high-energy-physics group has excellent technical facilities and support staff to perform this R&D. The group includes an electrical engineer and three electronics technicians plus a mechanical engineer and four mechanical technicians (all supported by our DoE base grant).

We anticipate no new manpower requirements to complete the proposed R&D.

### 5.3 Proposed Budget for FY94

Table 2: The proposed R&D budget for FY1994.

	Item	Cost
A.	Equipment	
1.	Two Hamamatsu R3809U MCP-PMT's	\$22k
2.	Fibers and test equipment for time-of-flight studies	\$8k
3.	Evaporator + vacuum system for $50 \times 50$ cm <sup>2</sup> areas	\$25k
4.	Ancillary equipment for fast RICH prototypes	\$5k
B.	Materials and Supplies	
1.	Electronic and optical components for time-of-flight studies	\$5k
2.	Electronic and optical components for aerogel studies	\$4k
3.	Electronic and optical components for fast RICH studies	\$4k
C.	Travel to test beams, likely at TRIUMF	\$6k
D.	Indirect Costs (59%) on items B and C	\$11k
	<b>Total</b>	<b>\$80k</b>

### 5.4 Milestones

#### 5.4.1 Time-of-Flight System

1. Studies of the proposed time-of-flight system are driven by procurement of the Hamamatsu R3809U MCP-PMT's, which devices have delivery of 60 days a.r.o. We designate the arrival date of these MCP-PMT's as  $t_0$ .
2. Prior to  $t_0$ : Procurement of silica fibers and measurement of their transparency; submission for the RFQ for custom MCP-PMT's.
3.  $t_0 + 1$  month: verification of timing performance of the MCP-PMT's with a laser setup.
4.  $t_0 + 2$  months: study of timing resolution of MCP-PMT's + fiber radiator using cosmic rays and radioactive sources.
5.  $t_0 + 3 - 4$  months: study of timing resolution of MCP-PMT's + fibers using a test beam, possibly at TRIUMF.

At this time the basic quality of the MCP-PMT time-of-flight system should be demonstrated.

#### 5.4.2 Aerogel + CsI Threshold Čerenkov Counters

1. Studies of the proposed aerogel system are driven by procurement of the aerogel samples. It is unclear to us how long it would take for such samples to arrive, although we understand that a fabrication cycle is about 3-4 weeks. We seek reasonable priority in negotiations between the SLAC *B*-Factory Collaboration and LLNL for delivery of aerogel samples. We designate the arrival date of the first aerogel samples as  $t_0$ .
2.  $t_0 + 1$  month: measurement of the UV-transparency of the samples.  
If they are sufficiently transparent, we could proceed to the following step. If not, we either attempt to procure higher-quality samples, or abandon the option of aerogel + CsI photocathodes.
3.  $t_0 + 3$  months: Presuming the first samples are of sufficient quality, we would take delivery of larger aerogel samples and incorporate these in prototype chambers with CsI photocathodes.
4.  $t_0 + 4$  months: Complete tests of the prototype chambers with our vacuum spectrophotometer and cosmic rays.
5.  $t_0 + 5 - 6$  months: Complete beam tests of the prototype chambers.  
In a favorable scenario, the proof of principle of the aerogel + CsI photocathode option would be available at this time.

#### 5.4.3 RICH Detectors with CsI Photocathodes

R&D on this option is ongoing:

1. Feb. 1994: Complete modifications to the existing 8" prototype chamber for use with a wire anode and larger gap. Study performance of this chamber with our vacuum spectrophotometer.  
Studies of turn-on transients and aging are proceeding throughout the entire R&D period.
2. March 1994: Complete the readout of the 8" chamber with Amplex chips. Complete substitution of G-10 chamber components by ceramic components.
3. April 1994: Bench tests of the ceramic chamber components, followed by beam tests at TRIUMF (pending the TRIUMF schedule).  
Begin construction of the  $50 \times 50$  cm<sup>2</sup> evaporation system and prototype chambers.
4. May-Oct. 1994: Studies of the larger-area prototype chambers.  
By Oct. 1994 the proposed round of prototype studies should be complete. However, a decision to implement a large-scale system may still require additional R&D.